AIChE

Analysis of the Advection–Diffusion Mixing by the Mapping Method Formalism in 3D Open-Flow Devices

Oleksandr Gorodetskyi, Michel F.M. Speetjens, and Patrick D. Anderson
Materials Technology, Eindhoven University of Technology, Eindhoven 5600 MB, The Netherlands

Massimiliano Giona
Dip. Ingegneria Chimica Materiali Ambiente, La Sapienza Università di Roma, via Eudossiana 18,
Roma 00185, Italy

DOI 10.1002/aic.14291
Published online November 30, 2013 in Wiley Online Library (wileyonlinelibrary.com)

This article extends the analysis of laminar mixing driven by a chaotic flow in the presence of diffusion to three-dimensional open-flow devices by means of the mapping-matrix method. The extended formulation of the mapping matrix recently proposed by Gorodetskyi et al. (2012) allows inclusion of the molecular diffusion in the mixing process. This provides an efficient numerical tool for understanding the interplay between a chaotic advective field and diffusion, especially for high Péclet numbers. As a prototypical open-flow device we consider the partitioned-pipe mixer. Results deriving from the application of the extended mapping method are compared with Galerkin simulations, and a close agreement is found. Short-term properties in the evolution of the concentration and the effect of axial diffusion are also addressed. © 2013 American Institute of Chemical Engineers *AIChE J*, 60: 387–407, 2014
Keywords: chaotic advection, diffusion, mixing simulations, spectral analysis, mapping method

Introduction

Mixing of fluids is highly important and widely spread phenomenon, ubiquitously occurring both in natural and artificially created processes.[1,2] Fluid mixing impacts on a variety of different fields, covering science, industry, everyday life and so forth. Our attention is mainly focused on the analysis of mixing related to process industry applications, where the final homogenized fluid mixture is the outcome of mixing units that operates either using stirring parts (impellers) or using complex static geometrical structures that modify the flow configuration (static mixers).[3] Mixing process appreciably depends on the flow conditions and on the geometric structure of the mixing device. In many cases, mixing is associated with turbulent motion, for which turbulent fluctuations enhance fluid mixing.[4] However, mixing of highly viscous fluids, usually associated with polymer and pharmaceutical processing,[5–7] represents another class of problems where mixing occurs in purely laminar conditions and often the resulting flows are Stokesian. This means that the spatial structure of the velocity field profile does not depend on the viscosity. In such problems, the efficiency of mixing is determined by the repeated stretching and folding of material lines and surfaces due to advective transport of fluid volumes.[8,9] The stretching and folding mechanism is enhanced if the flow induces Lagrangian chaos in the kinematics of fluid particles.[9,10] As thoroughly addressed by a huge literature in the last 30 years, laminar chaotic mixing provides a powerful alternative to turbulent flows.[11–13] Stretching and folding cause rapid reduction of the characteristic size of zones filled by uniform component, thus increasing the interfacial contact area.[14,15] This leads to the formation of zones with small-scale structures, in which molecular diffusion becomes highly efficient and drives the homogenization process.

Direct analysis of the advection–diffusion problem is computationally expensive, especially when the geometry of the mixing device is complex, as for static mixers, so there is a significant motivation for developing numerical tools for investigating advection–diffusion mixing that can be applied to complex flows and generic mixing devices. A variety of numerical methods has been developed for the investigation, description, and optimization of mixing in different flow devices.[16–19]

Focusing attention on static mixers, the flow device consists in a set of periodic units, and the same stretching and folding protocol of material elements repeats in every unit. For such flows (i.e., for flows possessing either spatial or time periodicity), Spencer and Wiley[20] proposed a method that describes transport of a conservative quantity from one state to another by means of a discretized mapping represented, on a finite mesh, by a matrix $\mathbf{\Phi}$. Mapping method has proved its efficiency in analysis of mixing and has been applied for variety of flows (mixers) that reflect realistic mixing in industry.[21–27]

The method is essentially based on the accurate tracking of a set of particles for specified interval of time or space. The flow domain is subdivided into small cells that are filled

---

Correspondence concerning this article should be addressed to P. D. Anderson at P.D.Anderson@tue.nl.

© 2013 American Institute of Chemical Engineers

with particles. The study is restricted to periodic flows, with period T_p (in time or space). Time-integration Runge–Kutta scheme is used to advect particles from initial state to their final position at the end of the period. The results of tracking are stored into the mapping matrix. The entries of the mapping matrix represent the fractions $\mathbf{\Phi}_{ij}=\frac{M_{ij}}{M_j}$ of markers M_j from donor cell Ω_j donated after one period T_p to the other parts of the domain, in particular to the recipient cell Ω_i that received M_{ij} markers. The mixture concentration is described by the N-th dimensional vector $\boldsymbol{C}$ that represents the coarse-grained description of the volume fraction (dimensionless concentration) and each component describes the concentration locally averaged in the associated cell, where N is the number of cells in the domain. The mapping matrix so constructed allows to compute redistribution of concentration $\boldsymbol{C}_n$ after n period of mixing for any arbitrary initially specified concentration $\boldsymbol{C}_0, \boldsymbol{C}_n=\underbrace{(\mathbf{\Phi}(\mathbf{\Phi}(...(\mathbf{\Phi}}_{n\text{times}}\boldsymbol{C}_0)...)))$. Constructed by such procedure mapping matrix concerns purely advective transport and once computed can be applied to describe the evolution of the concentration field starting from an arbitrary initial configuration of the fluid mixture.

There is a major conceptual limitation of the mapping method described above, which becomes physically relevant especially when applied to practical industrial devices. It describes the pure kinematics, thus neglecting the influence of molecular diffusion. The advective formulation of the mapping matrix approach has been recently extended by Gorodetskyi et al.,[28] by including the effects of, molecular diffusion in the construction of the matrix. The method is based on the stochastic formulation of advection–diffusion kinematics and on the analogy between stochastic differential equations and advection–diffusion dynamics. Moreover, Gorodetskyi et al. have shown that the purely advective mapping matrix can be interpreted in a new quantitative way. Coarse-graining acts essentially as an additional superimposed diffusional contribution, and purely advective analysis, performed using the advective mapping matrix, provides a reliable approximation for the advection–diffusion operator, essentially as a consequence of numerical diffusion induced by the coarse-graining. The effect of the numerical diffusion in the mapping formulation of chaotic mixing for extremely large Péclet values were studied by Gorodetskyi et al.[28,29]

The aim of this manuscript is to extend the mapping matrix formulation in the presence of diffusion to open-flow devices and static mixers. As a test-case, we consider a classical prototypical model, namely the partitioned-pipe mixer (PPM).

The physics of the homogenization process can be easily interpreted both as regards of homogenization time- and length-scales, and the spatial patterns associated with partially mixer structures, by considering the eigenvalues/eigenfunctions of the advection–diffusion operator, or equivalently of the mapping matrix.

Spectral (eigenvalue/eigenfunction) analysis has found a wide application in investigation of distributive mixing. Governing advection–diffusion equation is linear and thus amenable to characterization in terms of the eigenvalues and eigenvectors of the evolution operator.[30] Spectral structures, associated with the advection–diffusion operator, represent the backbone around which the evolution of a concentration field evolves due to the action of advection and diffusion. Spatial structure of the decaying scalar field rapidly becomes dominated by the slowest-decaying eigenmode, termed "strange eigenmode" Pierrehumbert,[31] to which many studies have been dedicated.[18,32–37]

In Refs. 18 and 38, analysis of the strange eigenmodes of advection–diffusion operator in two-dimensional (2-D) laminar chaotic flows has been performed. The connection between the spectral properties of the mapping matrix and the advection–diffusion operator has been revealed by Singh et al.[39] on the purely advective limit of the scalar transport.

The article by Gorodetskyi et al.[28] provides a platform for including the effect of molecular diffusion within the mapping-matrix formalism. This article develops the analysis by considering a prototypical toy-model, namely the time-periodic sine flow (TPSF) defined on the 2-D torus.[40] In the present article, we extend the theory and the application of the diffusive mapping matrix from simple 2-D flow to more complicated, realistic 3-D open flows, using the PPM as a prototypical system.

The inclusion of diffusion in the classical kinematic formulation of the mapping method gives a valuable contribution in the investigation of mixing problems, providing a closer correspondence between simulations and experiments, that is, the "real" advective-diffusive mixing, where diffusion is the ultimate driving force to homogenization. This allows a much more accurate prediction of the outcome of a mixing process, hereby reducing time and energy costs when real industrial devices have to be analyzed. Conversely, spectral analysis of the diffusive mapping matrix allows detailed investigation of the interaction between advective and diffusive transport in the fluid mixing, giving a clear understanding of the role of the diffusion and its influence on the results of the mixing.

Extension of the Mapping Method to Advective-Diffusive Transport

Diffusive mapping matrix

The original mapping method concerns purely advective transport. The inclusion of molecular diffusion within the method extends its domain of application and allows the investigation of realistic mixing devices.

The Lagrangian motion of a passive fluid particle in a d-dimensional flow domain $\mathcal{M}$ is affected by two factors: the advective contribution associated with a given stirring mechanics described by a velocity field $\mathbf{v}(\mathbf{x},t)$, and the influence of random fluctuations at a molecular level that, in a continuum Eulerian formulation, give rise to diffusive Fickian fluxes.

At a microscopic level, the interplay between advection and diffusion is thus described by the nondimensional stochastic differential equation[41,42]

$$d\mathbf{x}(t)=\mathbf{v}(\mathbf{x}(t),t)dt+\sqrt{\frac{2}{\mathrm{Pe}}}d\boldsymbol{\xi}(t), \tag{1}$$

where $\mathbf{v}(\mathbf{x})$ is the nondimensional velocity field, and $d\boldsymbol{\xi}(t)$ are the infinitesimal increments of a d-dimensional Wiener process ($d=2,3$ is the dimension of the flow-domain), that is, of a vector-valued stochastic process $\boldsymbol{\xi}(t)=(\xi_1(t), \ldots, \xi_d(t))$ in which $\xi_h(t)$ and $\xi_k(t)$ are one-dimensional (1-D) stochastic processes independent of each other for $h \neq k$, and possessing uncorrelated increments distributed in a normal way. Equation 1 is equipped with the initial condition $\mathbf{x}(0)=\mathbf{x}_0$.

Let $P(\mathbf{x}, t/\mathbf{x}_0)$ be the probability density function (pdf) associated with the stochastic process 1. For notational simplicity, we indicate this quantity as $P(\mathbf{x}, t)$, omitting the reference on the initial condition $\mathbf{x}_0$. The pdf $P(\mathbf{x}, t)$ satisfies the partial differential equation[42]

$$\frac{\partial P(\mathbf{x},t)}{\partial t} = -\nabla \cdot (\mathbf{v}(\mathbf{x},t)P(\mathbf{x},t)) + \frac{1}{\mathrm{Pe}}\nabla^2 P(\mathbf{x},t), \qquad (2)$$

that coincides with the classical nondimensional advection–diffusion equation, where Pe is the Péclet number.

The correspondence between the Lagrangian stochastic kinematics 1 and the Eulerian advection–diffusion equation 2 provides a straightforward method for extending the mapping techniques to account for molecular diffusion, by simply updating the construction. More precisely, the entries $\mathbf{\Phi}_{ij}$ of the diffusive mapping matrix are still given by $\frac{M_{ij}}{M_j}$, but M_{ij} is now the fraction of markers arriving at cell Ω_i from the initial cell Ω_j driven by the stochastic differential equation 1.

The stochastic differential equation 1 can be solved numerically by means of an Euler-Langevin explicit scheme.[42,43] Let h be the time step, $\mathbf{x}_n = \mathbf{x}(nh)$, and $\mathbf{v}_n(\mathbf{x}) = \mathbf{v}(\mathbf{x}, nh)$. The Euler-Langevin solver for Eq. 1 is simply given by

$$\mathbf{x}_{n+1} = \mathbf{x}_n + \mathbf{v}_n h + \sqrt{\frac{2}{\mathrm{Pe}}} h^{1/2} \mathbf{r}_n, \qquad (3)$$

where $\mathbf{r}_n = (r_{1,n}, \ldots, r_{d,n})$ is the realization of a d-dimensional normally distributed independent random variable. This means that the d random variables $r_{1,n}, \ldots, r_{d,n}$, are independent of each other and distributed according to a Gaussian distribution with zero mean and unit variance.

Open-flow devices

In the case of open-flow devices, such as static mixers, the steady state mixing properties are particularly interesting. Consider a generic static mixer obtained by the spatial repetition along the axial coordinate z of a given mixing unit, and suppose that the advecting field is steady. The velocity field consists of an axial component $w(\mathbf{x})$ along the coordinate z and of a transverse component $\mathbf{v}_\perp(\mathbf{x})$ along the transverse coordinates $\mathbf{x}_\perp = (x, y)$. Let us assume that nondimensional axial coordinate z has been obtained by rescaling the physical axial coordinate per the length of the fundamental mixing unit L, and the nondimensional transverse coordinates $\mathbf{x}_\perp$ are the physical coordinates of the transverse cross-section Σ_T of the mixing device divided by a characteristic transverse length W.

At steady state, the advection–diffusion equation for a nondimensional concentration-field $c(\mathbf{x})$ becomes

$$w(\mathbf{x})\frac{\partial c(\mathbf{x})}{\partial z} = -\mathbf{v}_\perp(\mathbf{x}) \cdot \nabla_\perp c(\mathbf{x}) + \frac{1}{\mathrm{Pe}}\nabla_\perp^2 c(\mathbf{x}) + \frac{1}{\alpha^2 \mathrm{Pe}}\frac{\partial^2 c(\mathbf{x})}{\partial z^2}. \qquad (4)$$

where the Péclet number $\mathrm{Pe} = t_\mathrm{diff}/t_\mathrm{adv}$ is the ratio of the characteristic diffusion time $t_\mathrm{diff} = W^2/D, D$ being the diffusion coefficient, and the characteristic advection time $t_\mathrm{adv} = L/V_0, V_0$ being a characteristic axial velocity. In Eq. 4 $\alpha = L/W$ is the aspect ratio, and is usually much larger than 1. Observe that the aspect ratio α in the advective contribution $-\mathbf{v}_\perp \cdot \nabla_\perp c$ has been included in the definition of the nondimensional transversal component $\mathbf{v}_\perp$.

If $\alpha \gg 1$, and Pe is sufficiently high, the contribution of axial diffusion is negligible, so that Eq. 4 simplifies as

$$w(\mathbf{x})\frac{\partial c(\mathbf{x})}{\partial z} = -\mathbf{v}_\perp(\mathbf{x}) \cdot \nabla_\perp c(\mathbf{x}) + \frac{1}{\mathrm{Pe}}\nabla_\perp^2 c(\mathbf{x}). \qquad (5)$$

As can be observed, Eq. 5 is formally very similar to the evolution equation for a closed-flow system, defined onto the transverse cross-section Σ_T, in which time t is replaced by the axial coordinate z, and the contribution of the first-order derivative $\partial c/\partial z$ is modulated by the axial velocity profile.

In this case, mapping analysis reduces to a coarse-grained description of the distributive action between the inlet $\Sigma_\mathrm{T,in}$ and the outlet cross-section $\Sigma_\mathrm{T,out}$ of the unit mixing modulus forming the static mixer. As $\Sigma_\mathrm{T,in}$ and $\Sigma_\mathrm{T,out}$ are identical ($\Sigma_\mathrm{T,in} = \Sigma_\mathrm{T,out} = \Sigma_\mathrm{T}$), let us sample these cross sections with a system of cells $\{\Omega_i\}$, and construct on Σ_T the entries of the inlet/outlet mapping matrix based on the partition $\{\Omega_i\}$. More precisely, the kinematic of an advecting-diffusing particle in the limit of negligible axial diffusion is given by

$$\begin{aligned} d\mathbf{x}_\perp(t) &= \mathbf{v}_\perp(\mathbf{x}_\perp(t), z(t))dt + \sqrt{\frac{2}{\mathrm{Pe}}} d\boldsymbol{\xi}_\perp(t), \\ dz(t) &= w(\mathbf{x}_\perp(t), z(t))dt, \end{aligned} \qquad (6)$$

where $\boldsymbol{\xi}_\perp(t) = (\xi_1(t), \xi_2(t))$. As an initial condition $\mathbf{x}_\perp(0) \in \Sigma_\mathrm{T,in}$, and $z(0) = 0$. The stochastic differential equation 6 is integrated unless at a time t^*, $z(t^*) \in \Sigma_\mathrm{T,out}$, and the corresponding value of the transversal coordinate $\mathbf{x}_\perp(t^*)$ is used to estimate M_{ij} starting from an ensamble of initial transversal position lying in Ω_j.

In a similar way, if axial-diffusion is accounted for, the same computational strategy is used, but the stochastic dynamics for fluid particles is given by

$$\begin{aligned} d\mathbf{x}_\perp(t) &= \mathbf{v}_\perp(\mathbf{x}_\perp(t), z(t))dt + \sqrt{\frac{2}{\mathrm{Pe}}} d\boldsymbol{\xi}_\perp(t), \\ dz(t) &= w(\mathbf{x}_\perp(t), z(t))dt + \sqrt{\frac{2}{\alpha^2 \mathrm{Pe}}} d\xi_z(t), \end{aligned} \qquad (7)$$

where $\xi_z(t)$ is a 1-D Wiener process uncorrelated from the 2-D transverse process $\xi_\perp(t)$. It can be observed, that the stochastic construction of the diffusive mapping matrix in the presence of axial diffusion—Eq. 7—does not require the enforcing of any boundary condition at the inlet/outlet cross section. Indeed, it corresponds to the propagation of the concentration field along the static mixer as if it was infinitely extended.

The diffusive mapping matrix is a stochastic vector-valued variable in itself, as its entries are the outcome of a stochastic process. To obtain a stable averaged quantity, N_p particles are placed (uniformly distributed) within each donor cell of the construction process. For large values of N_p, the diffusive mapping matrix so constructed converges toward the inlet/outlet propagator of the advection–diffusion equations (for values of Pe at which the effect of numerical diffusion is negligible with respect to molecular diffusion—see next paragraph). In the present case, a preliminary analysis showed that $N_p = 10^2$ is sufficient for obtaining stable averaged diffusive matrices.

In the numerical integration of Eqs. 6 and 7 via the Euler-Langevin scheme (Eq. 3), we use $h = 10^{-2}$, and reflection conditions for the particle trajectories at the solid walls of the device.

Effect of numerical diffusion

In the article by Gorodetskyi et al.,[28] it has been shown that coarse-graining in the mapping formalism acts as a superimposed diffusive contribution that adds to the mixing process. Quantitatively, the effect of numerical diffusion can be expressed by introducing an effective Péclet number $\mathrm{Pe}_{\mathrm{eff}}$. By definition, for a given mesh, the effective Péclet number is the value of the Péclet number associated with the purely advective mapping matrix and is a consequence of coarse-graining. For triangular meshes (as well as for structured ones) of increasing resolution (i.e., for increasing N_c), $\mathrm{Pe}_{\mathrm{eff}}$ is a function of the linear lattice size of the mesh[28,29]

$$\mathrm{Pe}_{\mathrm{eff}} \simeq p_0 N_c^2, \tag{8}$$

where the prefactor p_0 is constant and depends on the flow protocol, and $N_c = 1/\Delta x$, where Δx is the linear size of the element in the mesh. In this article, we use equilateral triangular mesh. Elements are aligned with rigid physical horizontal and vertical boundaries of the mixer. An example of low-rank mesh, that consists of 790 elements and corresponds to lattice size $\Delta x = 0.1$, is depicted in Figure 1. Unstructured triangular mesh is generated using Gambit. As the cross-section Σ_{T} is 2-D, the quantity N_c^2 is proportional to the total number of cells used in the construction of the mapping matrix.

Therefore, for any mesh, the diffusive mapping matrix describes an advection–diffusion process acting at a value $\overline{D}$ of the diffusivity, where $\overline{D}$ is the sum of the molecular diffusivity D and of the numerical diffusion coefficient D_{num}. Correspondingly, the actual Péclet number $\overline{\mathrm{Pe}}$ is $\overline{\mathrm{Pe}}^{-1} = \mathrm{Pe}^{-1} + \mathrm{Pe}_{\mathrm{eff}}^{-1}$, where $\mathrm{Pe}_{\mathrm{eff}} = W^2/D_{\mathrm{num}}$ is the Péclet number associated with D_{num}.

Equation 8 provides the quantitative characterization of numerical diffusion generated by coarse-graining. It allows application of the purely advective mapping method for studying transport in chaotic flow, making direct connection between the analysis of advective mapping matrix and the properties of the advection–diffusion equation.

The effect of numerical diffusion can be appreciated by considering the characteristic decay rate toward the uniform, fully homogenized profile. Let λ_2 be the second dominant eigenvalue of the mapping matrix (the first eigenvalue equals 1 by mass conservation). Along the static mixer, any integral norm $N[c](z)$ (such as the square-root of the variance) associated with the concentration field c evaluated at the value z of the axial abscissa decays for generic initial condition as

$$N[c](z) \simeq I_0 e^{-\Lambda z}, \tag{9}$$

where Λ is referred to as the dominant decay exponent. Let Λ_{mp} be the mapping-matrix approximation of Λ. The quantity Λ is related to λ_2 by the equation

$$\Lambda = -\frac{\log|\lambda_2|}{T_{\mathrm{p}}} \tag{10}$$

where $|\lambda_2|$ is a magnitude of the second dominant eigenvalue and T_{p} is the spatial period of the flow.

From the spectral (eigenvalue) analysis of the mapping matrix, it is possible to determine the value of the prefactor p_0. This calculation has been developed by Gorodetskyi et al.,[28] and it is not repeated here. Below the final result is succinctly reported, as it is relevant for the further analysis of mixing in open-flow systems.

Let us consider a flow system for which, over a consistent range of Péclet number values, the dominant decay exponent $\Lambda(\mathrm{Pe})$ decays as a power law

$$\Lambda(\mathrm{Pe}) \simeq \Lambda_0 \mathrm{Pe}^{-\beta}, \tag{11}$$

where Λ_0 is a constant and $\beta \in [0,1]$. As discussed in Ref. 38 and in the subsequent literature, the occurrence of the scaling law 11 for the dominant decay exponent is a generic feature of laminar chaotic and nonchaotic mixing systems. This typical behavior characterizes also the spectral properties of advecting-diffusing dynamics in PPM protocols, as discussed in later paragraph.

Let us indicate with $\Lambda_{\mathrm{mp}}(\mathrm{Pe}; N_c)$ the dominant decay exponent of the diffusive mapping matrix at a value Pe of the Péclet number for a mesh resolution N_c, and with $\Lambda^c_{\mathrm{mp}}(N_c)$ the corresponding quantity of the purely advective mapping matrix for the same mesh resolution N_c. Then, the prefactor p_0 can be estimated numerically from the equation[28]

$$\Lambda_{\mathrm{mp}}(\mathrm{Pe}; N_c) = \Lambda^c_{\mathrm{mp}}(N_c) \left(\frac{p_0 N_c^2}{\mathrm{Pe}} + 1 \right)^{\beta}. \tag{12}$$

The value of the scaling parameter β can be obtained directly from the analysis of purely advective mapping matrices.[28] Values of Λ_{mp} are determined from the diffusive mapping matrix and Λ^c_{mp} from purely advective mapping matrix according to Eq. 10. Therefore, Eq. 12 defines a single-parameter curve, relating $\Lambda_{\mathrm{mp}}(\mathrm{Pe}; N_c)$ to Pe, for fixed N_c, that is, for a given mesh, in which the only unknown parameter is just the prefactor p_0. Determined for a coarse mesh, prefactor p_0 remains fixed for a finer mesh at the same flow protocol. The graphs of Eq. 12 for several typical PPM protocols discussed further.

From the definition of the effective Péclet number and from Eqs. 8 and 12, it follows that $\mathrm{Pe}_{\mathrm{eff}}$ is the value of the Péclet number (associated with molecular diffusion) at which the strength of numerical diffusion equals that of molecular diffusion. As a consequence, to keep numerical diffusion negligible with respect to molecular diffusion, the value of Pe should be at least one order of magnitude smaller than $p_0 N_c^2$.

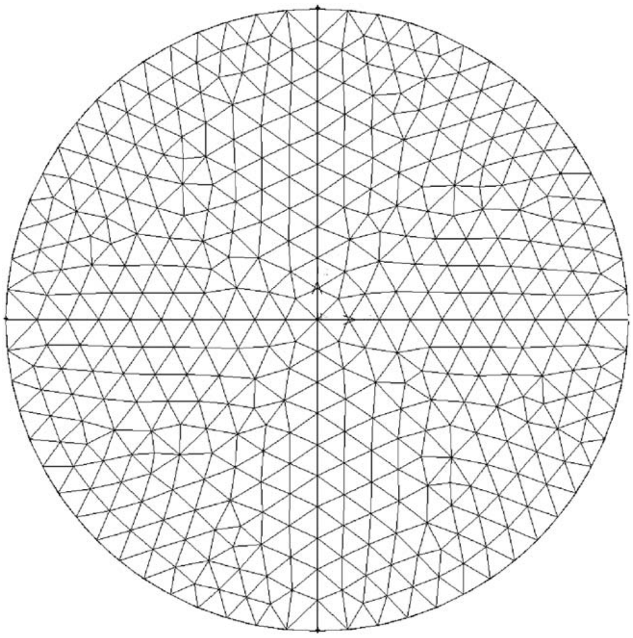

Figure 1. Typical triangular mesh used for simulations.

There is another major byproduct of the analysis developed in Ref. 28. In the case one is interested to very large Péclet values, it is computationally convenient to consider the purely advective mapping matrix for high mesh resolutions. Owing to numerical diffusion, it permits to simulate advection–diffusion processes at a value of Pe corresponding to the effective Péclet number pertaining to the chosen mesh. As commonly $p_0 \simeq \mathcal{O}(10)$, for $N_c \geq 10^3$, it permits to simulate mixing dynamics for $\mathrm{Pe} = \mathrm{Pe}_{\mathrm{eff}} \geq 10^7$.

Problem Definition

Partitioned-pipe mixer

As a model of realistic, physically realizable, chaotic open-flow devices, we consider the PPM in the classical flow-field approximation proposed by Khakhar et al.[44] The PPM has been originally introduced as a simplified model mimicking the relevant qualitative features of the well-known Kenics static mixer.[24,25,45,46] It consists of a cylindrical pipe partitioned into a sequence of semicircular ducts by means of rectangular plates of length L fixed perpendicularly to each other (Figure 2).

The PPM model is essentially a three-dimensional (3-D) spatially periodic flow with period $2L$. It involves two superimposed, independent, flow fields: a cross-sectional (rotational) velocity field and a fully developed axial Poiseuille profile in each semicircular duct. Such partition enables the reduction of the 3-D flow to a 2-D mapping between the inlets of the periodic mixing units. The flow in semicircular ducts is induced by a constant pressure gradient and shear stresses caused by uniform rotation of the cylindrical wall with constant axial velocity Ω, while inner plates are fixed.

The approximate cross-section velocity field based on a one-term approximation of the stream function is given by[44]

$$v_r(r,\theta) = \beta_{\mathrm{ppm}}\, r(1-r^{\gamma})\sin 2\theta = \beta_{\mathrm{ppm}}\, \hat{v}_r(r,\theta)$$

$$v_\theta(r,\theta) = -\beta_{\mathrm{ppm}}\,(2-(2+\gamma)r^{\gamma})\sin^2\theta = \beta_{\mathrm{ppm}}\, \hat{v}_\theta(r,\theta)$$

where $\gamma \approx 0.915$.

The fluid dynamics and transport properties are controlled by a single parameter β_{ppm}, introduced by Khakhar et al.[44] as a "mixing strength"

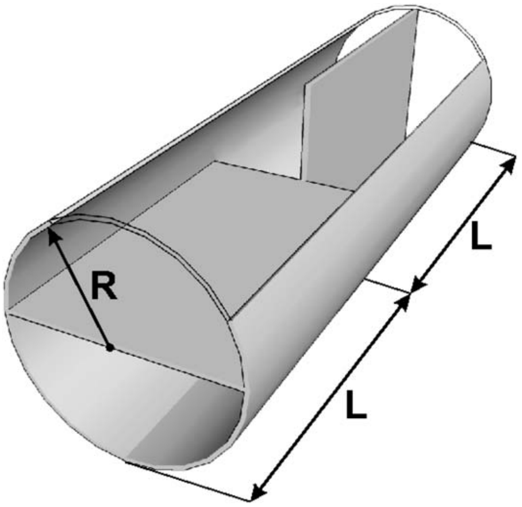

Figure 2. Schematic view of the PPM.

$$\beta_{\mathrm{ppm}} = \frac{4\Omega L}{3\gamma V_{\Delta p} R}, \tag{13}$$

where $V_{\Delta p}$ is the average axial velocity, and is a measure of the strength of the transverse velocity component with respect to the mean axial velocity.

The normalized axial flow is a pressure-driven flow in a semicircular duct, the expression of which in cylindrical coordinates reads

$$w(r,\theta) = \sum_{k=1}^{\infty}\left[\left(\frac{r}{R}\right)^{2k-1} - \left(\frac{r}{R}\right)^{2}\right]\frac{\sin[(2k-1)\theta]}{(2k-1)[4-(2k-1)^2]}. \tag{14}$$

The PPM flow possesses a complex structure that can be explored by considering the Poincaré sections of the Lagrangian dynamics associated with the kinematics of fluid elements and, as will be discussed below, by developing the spectral analysis of the mapping matrices built for different values of the parameter β_{ppm}.

Advective properties of PPM

PPM never accomplishes a globally chaotic state. Consequently, islands of regular motion always coexist with one or more chaotic regions.[44] Poincaré sections associated with the Lagrangian kinematics of fluid particles provide the simplest way to reveal chaotic and regular zones. Regular zones (also referred to as quasiperiodic islands) are invariant subsets, characterized by a vanishing maximum Lyapunov exponent. In the absence of the diffusion, owing to invariance, there is no material transfer from/to the quasiperiodic islands and the chaotic regions, that is, there is no material flux through the boundary of the islands. The purely kinematic description of mixing neglects this important feature (i.e., the material flux exchange between chaotic and regular regions), which controls the large-distance homogenization process in real mixing equipment.

In point of fact, one of the main motivations of this article is investigation of the material exchange through the boundaries due to the diffusion mechanism, *ipso facto* assigning the role of the diffusion in the mixing process.

The flow is spatially periodic in the axial direction. To build Poincaré sections, low resolution triangular mesh (equilateral triangles), that contains $N = 760$ elements, was selected (see Figure 1). In the center of each element a single particle is placed and tracked for 200 periods. Poincaré sections are generated as projection of all intersections after each periodic unit $z = 2kL\,(k = 0, 200)$, on the plane parallel to the surfaces. Poincaré section was built for several flow protocols and is depicted in Figure 3.

Poincaré sections exhibit a complex structure for all the values of the parameter β_{ppm}, with chaotic regions interspersed between regular islands. For small values of β_{ppm}, see Figure 3 panel *a* and *b*, regular islands of different sizes occupy almost the whole cross-section of the flow domain. Increasing β_{ppm}, larger quasiperiodic islands shrink in size and smaller structures disappear, see Figure 3 *d, e*. For $\beta_{\mathrm{ppm}} = 8$, the flow outside the two large islands seems to be chaotic almost everywhere. Increasing β_{ppm} to $\beta_{\mathrm{ppm}} = 10$, other large islands appear, reducing the extension of the chaotic region. Increase of β_{ppm} up to $\beta_{\mathrm{ppm}} = 20$ leads to a further decreasing of the size of the regular zones.

The inclusion of diffusion into the description of the mixing process gives qualitatively new results. Invariant for the purely advective transport, small-scale regular zones can be partially or completely destroyed, depending on the diffusivity of the

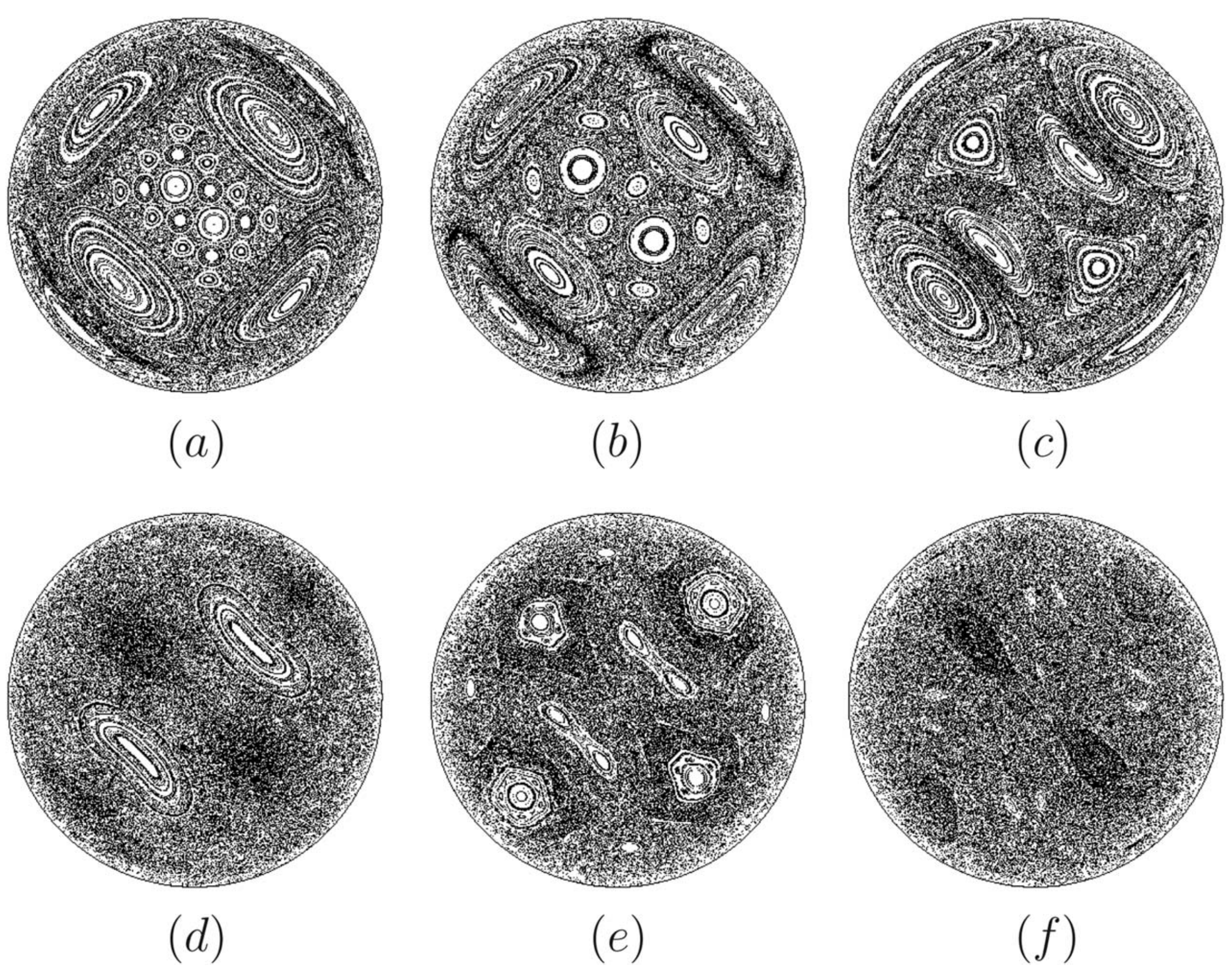

Figure 3. Poincaré sections for different values of mixing strength β_{ppm}. Panel (*a*) corresponds to $\beta_{ppm}=1$; (*b*)$\beta_{ppm}=2$; (*c*)$\beta_{ppm}=4$; (*d*)$\beta_{ppm}=8$; (*e*)$\beta_{ppm}=10$; (*f*)$\beta_{ppm}=20$.

mixing fluid that leads to a more realistic analysis of mixing than the purely kinematic analysis. These statements are sustained by the eigenmode analysis addressed in the next sections.

Quantification of the mixing quality

As a quantitative criterion for analysis of the mixture homogeneity, with the coarse-grained mapping formalism, the discrete intensity of segregation I_d is chosen.[21,47] It is computed on the discrete concentration field obtained by the mapping method and expressed as follows

$$I_\mathrm{d}=\frac{1}{\overline{C}}(1-\overline{C})\frac{1}{N}\sum_{i=1}^{N}(C_i-\overline{C})^2, \tag{15}$$

where C_i indicates the coarse-grained concentration in the i-th cell Ω_i, N is the total number of cells in the cross-section of the flow domain and $\overline{C}$ represents the average concentration

$$\overline{C}=\frac{1}{N}\sum_{i=1}^{N}C_i. \tag{16}$$

The intensity of segregation I_d is a measure of the deviation of the local concentration from perfectly mixed condition, which represents a homogeneous state of the mixture. The value of I_d is limited in the range $I_\mathrm{d}\in[0, 1]$. For completely segregated systems, $I_\mathrm{d}=1$. As the mixing process proceeds, the value of the intensity of segregation gradually decays to $I_\mathrm{d}=0$ reaching perfectly mixed state, when the concentration in each cell C_i equals the average concentration $\overline{C}$ in the flow domain.

The intensity of segregation is a coarse-grained quantity approximating the square of the L^2-norm $||c-\overline{c}||_{L^2}(z)$ of the zero-mean concentration field $c(\mathbf{x}_\perp, z)-\overline{c}$ in the continuum limit, evaluated on the cross-section Σ_T of the static mixer

$$\begin{aligned}\|c-\overline{c}\,\|^2_{L^2}(z) &= \int_{\sum_\mathrm{T}}(c(\mathbf{x}\perp,\mathrm{z})-\overline{c})^2 d\mathbf{x}_\perp, \overline{c}\\ &= \frac{1}{\mathrm{area}(\sum_\mathrm{T})}\int_{\sum_\mathrm{T}} c(\mathbf{x}_\perp d\mathbf{x}_\perp, z)d\mathbf{x}_\perp.\end{aligned} \tag{17}$$

Therefore, for large z and for generic initial conditions, I_d decays exponentially as a function of the axial coordinate z with an exponent twice as large as the dominant decay exponent Λ_mp

$$I_d(z)\sim e^{-2\Lambda_\mathrm{mp}z}. \tag{18}$$

The intensity of segregation, provides quantitative criteria to characterize the decay rate of concentration field along the axial coordinate, for settled inlet concentrations. A more general approach, independent of the initial conditions, for characterizing the decay rate of scalar fields can be grounded on the spectral properties of corresponding mapping matrices, and particularly on the analysis of dominant eigenmode(s) as a function of the Péclet number. This approach is thoroughly addressed in the next sections.

Advective-Diffusive Transport: Eigenmode Analysis of the PPM

In this section, the connection between the mixing properties and the eigenmodes obtained by the diffusive mapping matrix as a function of the Péclet number is investigated. The behavior of the dominant eigenvalues and the properties of the associated dominant eigenvectors are particularly relevant, as they control the asymptotic decay for large z.

To validate quantitatively, the diffusive mapping matrix approach, the comparison with the corresponding results obtained from the Galerkin expansion (see the Appendix for details) of the continuum advection–diffusion operator is performed. The analysis is developed by considering negligible axial diffusion. The influence of axial diffusion is addressed in separate paragraph.

Comparison with continuum advection–diffusion results

Due to the linearity of the advection–diffusion equation, the evolution of the concentration field is simply determined by the properties of the eigenvalue-eigenfunction spectrum associated with the advection–diffusion operator.[38] The detailed analysis of spectral properties of the advection–diffusion operator in the case of simple TPSF has been provided by Cerbelli et al.[38] In Ref. 28, Gorodetskyi et al. developed a quantitative comparative analysis of dominant decay exponent Λ obtained considering a Fourier-series expansion of the advection–diffusion operator and $\Lambda_{\rm mp}$ deriving from the diffusive mapping-matrix approach for the TPSF. The results so obtained showed that up to a critical Péclet number, which depends on the discretization, mapping method provides a reliable and accurate estimate for the eigenvalues of the advection–diffusion operator.

It is interesting to extend a similar analysis to more realistic flow, such as the PPM. The Appendix, added at the end of this manuscript, provides a succinct but comprehensive description of the Galerkin expansion of the advection–diffusion operator in the case of the PPM. As shown below, the comparative analysis of the dominant decay exponents (Λ vs. $\Lambda_{\rm mp}$) confirms the results obtained in Ref. 28 for the simpler TPSF, and support the claim that the diffusive mapping matrix approach is a robust and simple computational tool for predicting the spectral properties of the advection–diffusion operator, and ultimately for quantifying mixing processes in the presence of diffusion.

Figure 4 depicts the typical behavior of $\Lambda_{\rm mp}$ vs. the Péclet number Pe for the PPM flow at several values of $\beta_{\rm ppm}$, and compares it with the dominant decay exponent Λ in the continuum limit approach. Markers "◇", "○", "□", "△" correspond to different lattice size Δx of the mesh. Specifically, "◇" refers to Δx=0.1, "○" to Δx=0.05, "□" to Δx=0.05, and "△" to Δx=0.015. Markers "●" depict the results of the Galerkin expansion of the continuum advection–diffusion operator, by using the approach described in the Appendix.

For sufficiently large Pe values, the dominant decay exponent Λ follows a power-law dependence on Pe, described by Eq. 11. Therefore, Eq. 12 applies for describing the functional dependence of $\Lambda_{\rm mp}$ on Pe.

In all of the considered PPM protocol ($\beta_{\rm ppm}=1,4,8,10$), the values of $\Lambda_{\rm mp}$ practically coincides with Λ up to a given critical Péclet number, approximately equal to ${\rm Pe}_{\rm eff}/10$, that depends on N_c. Increasing Péclet number, $\Lambda_{\rm mp}$ saturates toward $\Lambda^c_{\rm mp}$ of a purely advective case as predicted by Eq. 12.

As can be observed from the description developed in the Appendix, the computational analysis of PPM by means of a direct Galerkin expansion of the advection–diffusion operator is extremely onerous and its practical implementation is time-consuming. Its practical application is further limited to values of the Péclet numbers (Pe $\sim 10^5$) as for higher Pe value the resolution of the spatial concentration gradients requires the inclusion of a very large number of modes in the Fourier expansion, making the direct Galerkin approximation practically prohibitive. We use $N_{\rm F}=50$ for Pe $< 10^2$ up to $N_{\rm F}=120$ for Pe $=2\times10^4$ and higher, corresponding to a total number of Fourier modes $[(N_{\rm F}+1)^2]$ ranging from 2601 up to 14,641. Nevertheless, the dominant decay exponent Λ for large Péclet values finds an accurate approximation by $\Lambda_{\rm mp}$ simply by refining mesh resolution.

For a given mesh structure and a given flow protocol, the prefactor p_0 entering Eq. 8 can be estimated (the numerical analysis of prefactor p_0 for different protocols of the PPM flow is addressed in next section). Consequently, the value of the effective Péclet number can be predicted, and by simply implementing the purely advective mapping matrix for increasing mesh resolutions (increasing N_c) it is possible to make an accurate estimate of the spectral properties of the continuum advection–diffusion operator.

Figure 5 depicts the comparison of $\Lambda^c_{\rm mp}$ (dots ●") and Λ (dots "○") as a function of the effective Péclet number for four typical protocols of the PPM flow. Comparing $\Lambda^c_{\rm mp}$ and Λ, we set ${\rm Pe}={\rm Pe}_{\rm eff}$ for the data obtained by using the purely advective mapping matrix. Modulation of the advective-diffusive process at low Péclet numbers via purely advective mapping matrix requires very coarse mesh, that eventually effects accuracy of the spectral results. To validate a mapping approach data from diffusive mapping matrix ($\Lambda_{\rm mp}$) is considered (markers"+").

This comparative analysis shows an excellent quantitative agreement between $\Lambda^c_{\rm mp}$ obtained from the purely advective mapping matrix and Λ associated with the continuum advection–diffusion operator.

Table 1 review the values of the scaling exponent β defined by Eq. 11 for the PPM flow protocols considered. As can be observed, for $\beta_{\rm ppm}=4$ and $\beta_{\rm ppm}=10$, a crossover phenomenon occurs, namely as Pe increases the power law scaling shifts to higher values of β. For example, in the case of $\beta_{\rm ppm}=10$, one observes the scaling $\Lambda \sim {\rm Pe}^{-\beta_1}$ with $\beta_1=0.56$ in the range ${\rm Pe} \in (2\times10^2, 5\times10^3)$, while for higher ${\rm Pe} \in (6\times10^3, 10^6), \Lambda \sim {\rm Pe}^{-\beta_2}$ with $\beta_2=0.83$. This crossover phenomenon seems to be a generic property of advection–diffusion operator in partially chaotic flows (i.e., in flows possessing quasiperiodic islands of nonvanishing measure), as thoroughly addressed in Ref. 29. More precisely, a thorough analysis developed in Ref. 29 for prototypical model flows up to Pe $=10^8$ have shown that in the presence of quasiperiodic islands the dominant decay exponent eventually sets into a purely diffusive scaling $\Lambda \sim {\rm Pe}^{-1}$ (starting from Pe $\simeq 10^7$ or higher), and that the associated eigenfunction becomes fully localized on the quasiperiodic islands.

The analysis developed above for the dominant eigenmode can be extended to the higher-order eigenvalues. Figure 6 provides an analogous comparison for Λ_k deriving from the Galerkin expansion and $\Lambda^c_{{\rm mp},k}$ associated with the purely advective mapping matrix for the third ($k=3$, markers "□"

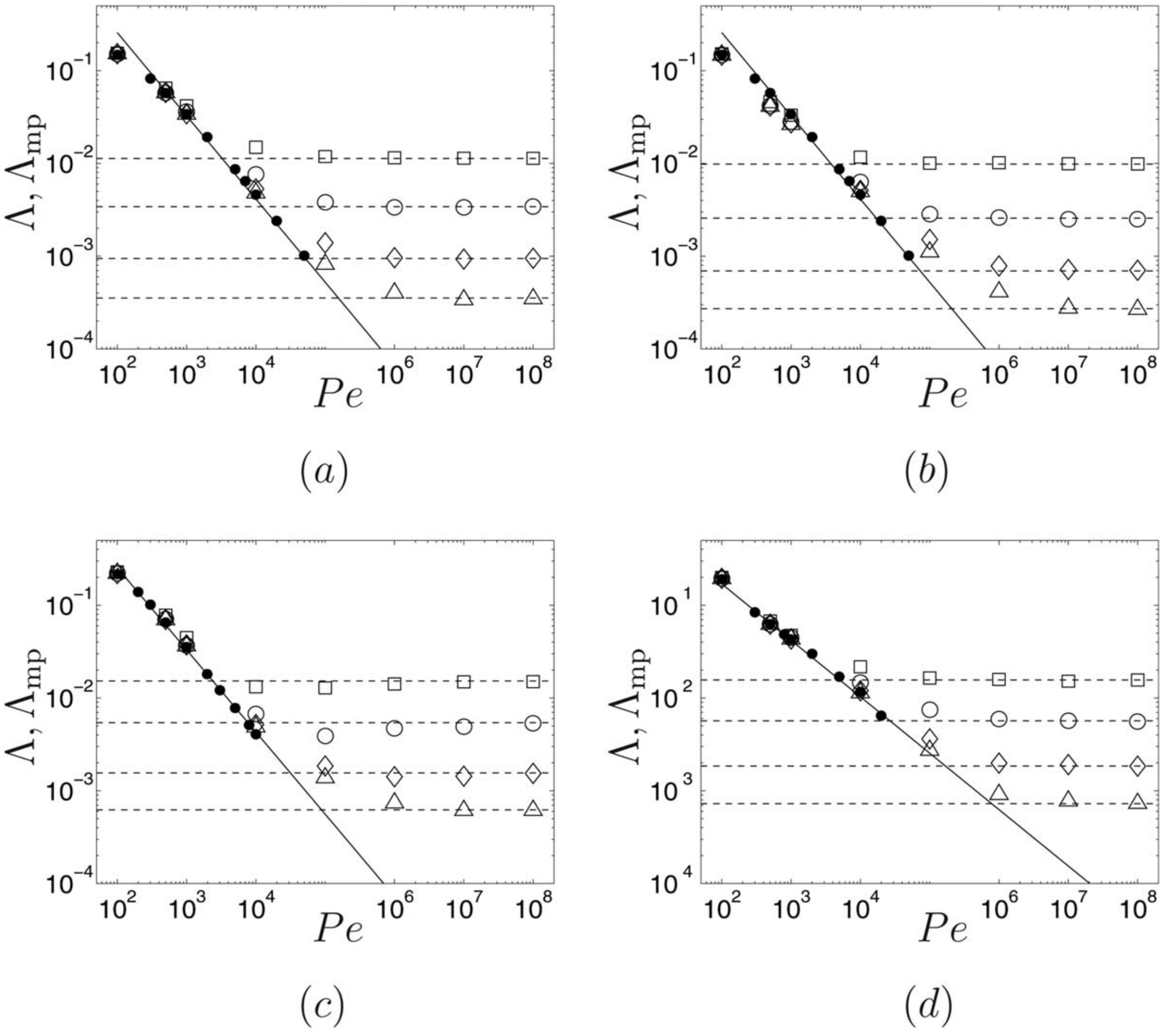

Figure 4. Dominant decay exponent of the diffusive mapping matrix Λ_{mp} (markers "◇," "○," "□," "△" correspond to different mesh resolution) and Λ (dots "●") vs. Pe at $\beta_{ppm} = 1$ panel (*a*); $\beta_{ppm} = 4$ panel (*b*); $\beta_{ppm} = 8$ panel (*c*); $\beta_{ppm} = 10$ panel (*d*).

Solid lines represent the scaling of the dominant decay exponent Λ of the advection–diffusion equation, dotted horizontal lines correspond to the limit values Λ^{c}_{mp} of the purely advective case.

and "■"); fifth ($k = 5$, markers "◇" and "◆"); tenth ($k = 10$, markers "△" and "▲") eigenmodes. The associated decay exponents Λ_k and $\Lambda^{c}_{mp,k}$ are obtained according to Eq. 10, replacing λ_2 with $|\lambda_k|$, where $k = 3, 5, 10$. According to this notation, $\Lambda = \Lambda_2$. The quantitative agreement between Λ_k and $\Lambda^{c}_{mp,k}$ for higher-order eigenmodes, indicates that the purely advecting mapping simulation are able to capture all the relevant spectral structure of the advection–diffusion operator, thus providing a reliable approximation for its global dynamics. It further indicates that the purely advective mapping method is a powerful and computationally highly efficient (compared to the direct analysis of the advection–diffusion operator) alternative to investigate advective-diffusive transport problems for high Péclet values, which can be applied without difficulty to realistic models of industrially used static mixers.

Estimate of numerical diffusion

As addressed in previous section, the dominant decay exponent Λ_{mp} obtained from the diffusive mapping analysis provides an accurate estimate of the dominant decay exponent Λ of the advection–diffusion operator up to a critical Pe value, proportional to the effective Péclet number. This is due to the fact that coarse-graining induces a "zero-level diffusivity" by discretization, the intensity of which is expressed by the nondimensional number $\mathrm{Pe}_{\mathrm{eff}}$, which superimposes to molecular diffusion.

This section addresses the estimate of the effect of numerical diffusion, and how it depends on the mesh resolution and on the flow protocol. Thereby, the analysis is splitted in two cases: (a) at large Péclet values, the effect of molecular diffusion is completely overwhelmed by numerical diffusion and the spectral properties of the diffusive mapping matrix converge to those of the purely advective one; (b) at lower Péclet numbers molecular and numerical diffusion cope with each other, and their relative influence depends on the actual Pe value compared to the effective $\mathrm{Pe}_{\mathrm{eff}}$ quantifying the intensity of numerical diffusion.

Figure 7 shows the dependence of dominant decay exponent Λ_{mp} of the diffusive mapping matrix on the Péclet number, at different resolution of the flow domain. As the Péclet number Pe increases, for a fixed mesh resolution, the value of Λ_{mp} gradually converges toward the constant value Λ^{c}_{mp} that corresponds to purely advective case, denoted by dashed horizontal lines.

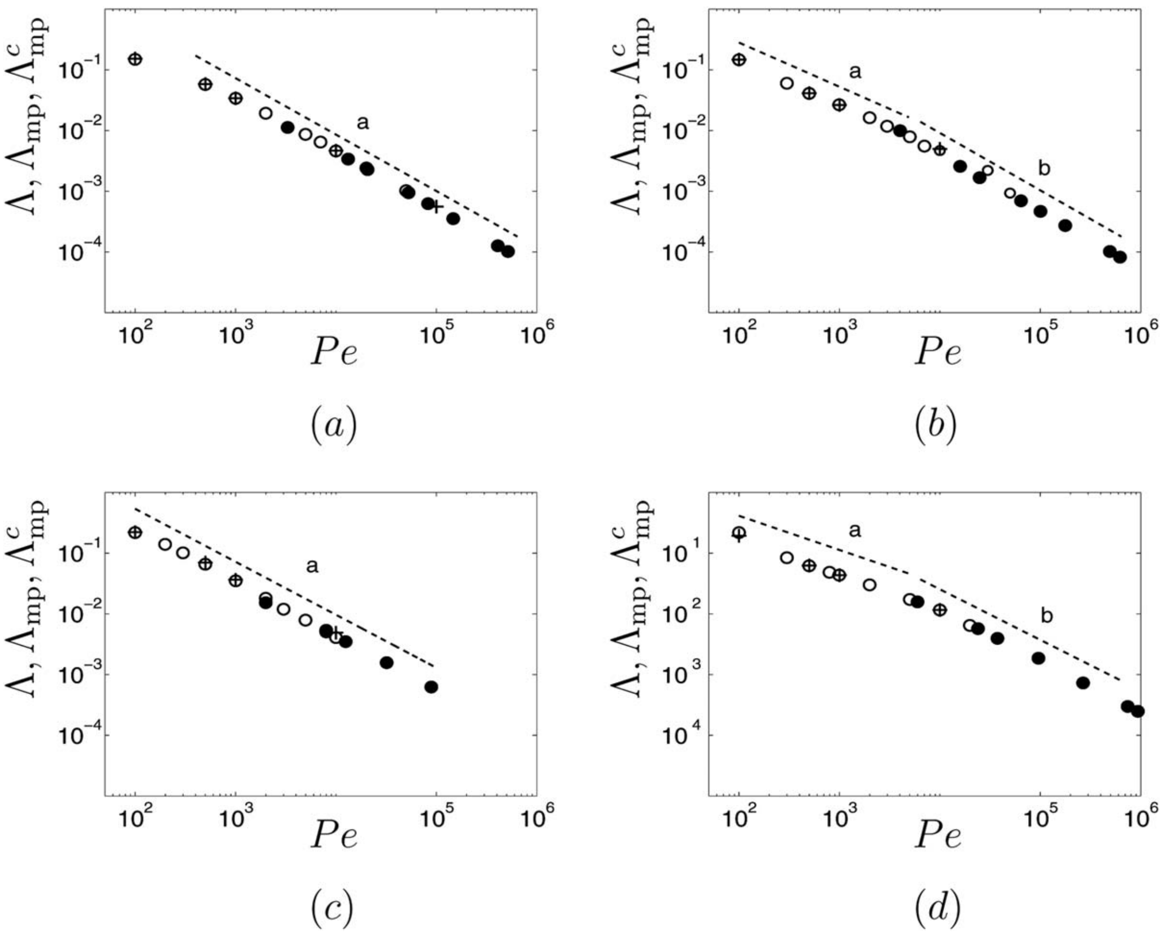

(a) (b)

(c) (d)

Figure 5. Comparison of the prediction for the dominant decay exponent by using the purely advective mapping matrix Λ_{mp}^c and Λ deriving from Galerkin expansion. Markers "●" refer to Λ_{mp}^c, "+" to Λ_{mp} and "○" to Λ.

Panel (*a*) refers to $\beta_{\mathrm{ppm}}=1$; panel (*b*) to $\beta_{\mathrm{ppm}}=4$; panel (*c*) to $\beta_{\mathrm{ppm}}=8$; and panel (*d*) to $\beta_{\mathrm{ppm}}=10$. The dotted lines (lines a and b in the case crossover phenomena occur) represent the scaling $\Lambda=\Lambda_{\mathrm{mp}}^c \sim \mathrm{Pe}^{-\beta}$.

The graphs of Λ_{mp} vs. Pe (solid lines in Figure 7) correspond to the curve expressed by Eq. 12, where the only unknown parameter is just the prefactor p_0. Therefore, p_0 can be determined using the curves depicted in Figure 7. To estimate the prefactor p_0, the dependence of Λ_{mp} on Pe was build for four different triangular meshes with different $\Delta x=N_c^{-1}$. Markers "□" correspond to a mesh with lattice size $\Delta x=0.1$ that contains 760 elements; "○" to $\Delta x=0.05$ and 2940 elements, "◇" to $\Delta x=0.025$ and 11,536 elements, and "△" to $\Delta x=0.015$ and 31,776 elements. Using data depicted in Figure 7 and Eq. 12, the prefactors p_0 for different protocols of PPM were determined by means of a one-parameter nonlinear regression. Table 2 reports the values of the prefactor p_0 so obtained for the PPM protocols considered.

As can be observed, the values of p_0 for the different PPM protocols are order of 10 and higher. This means that

Table 1. Scaling Exponent β Characterizing the Behavior of the Dominant Decay Exponent with Pe for Different Protocols of PPM

β_{ppm}	1	4	8	10
β	0.93	0.73 for Pe $< 5\times10^3$ 0.94 for Pe $> 5\times10^3$	0.87	0.56 for Pe $< 6\times10^3$ 0.83 for Pe $> 6\times10^3$

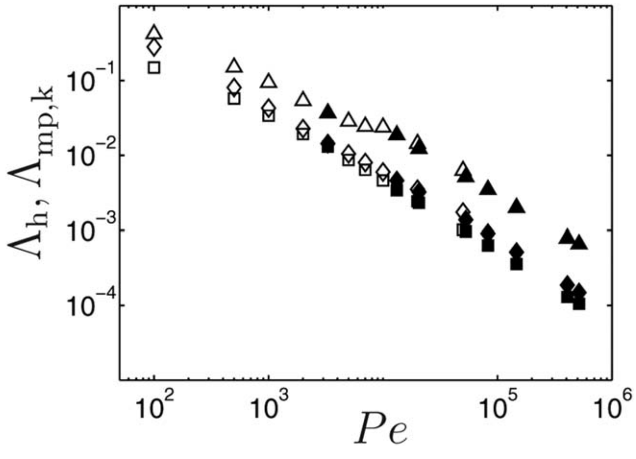

Figure 6. Decay exponents of the purely advective mapping matrix $\Lambda_{\mathrm{mp},k}^c$ vs. $\mathrm{Pe}_{\mathrm{eff}}$ (filled markers "■," "◆," and "▲") and Λ_k obtained from the Galerkin expansion of the advection–diffusion operator (empty markers "□," "◇," and "△") vs. $\mathrm{Pe}=\mathrm{Pe}_{\mathrm{eff}}$.

Index *k* indicates the order of the eigenmode. Markers "□" and "■" refer to the third (*k*=3), "◇" and "◆" to the fifth (*k*=5), "△" and "▲" to the tenth (*k*=10) eigenmode.

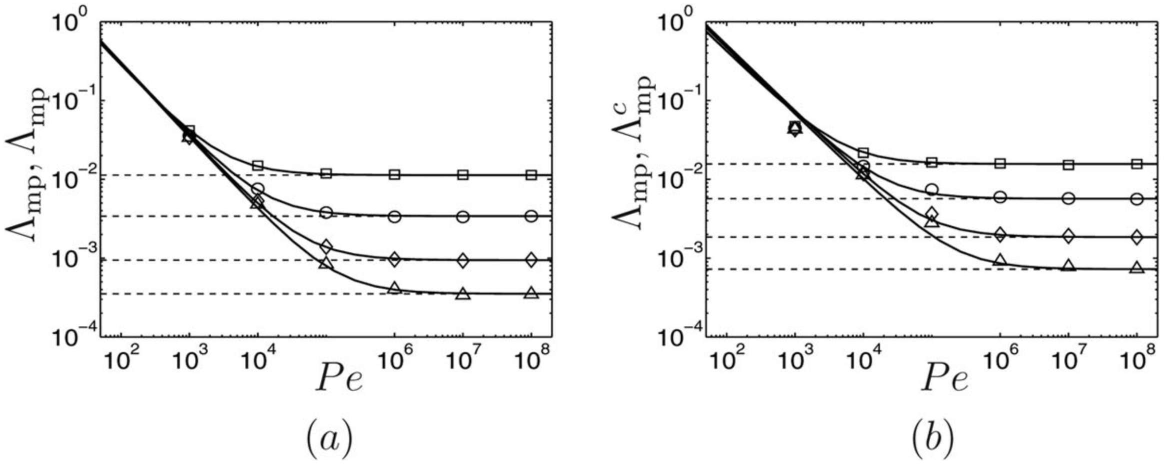

Figure 7. Dominant decay exponent $\Lambda_{\rm mp}$ vs. Pe for different resolution of the domain.

Panel (*a*) corresponds to the case $\beta_{\rm ppm}=1$, (*b*) to $\beta_{\rm ppm}=10$. Solid lines represent the graph of the curve expressed by Eq. 12.

by choosing a resolution of $N_c \simeq 10^3$ is it possible to reach values of the effective Péclet number of about 10^7-10^8, and use the purely advective mapping matrix to address in a reliable way laminar chaotic mixing for large Péclet values.

Axial diffusion

The extended mapping technique applied to open-flow devices is able to include the effect of axial diffusion, simply by replacing the stochastic differential equation 6 with Eq. 7. In the previous paragraphs, we have neglected this contribution, as in the overwhelming majority of practical devices the geometrical aspect ratio α is much greater than 10, and corresponding the influence of the axial diffusive terms is order of magnitude smaller than transverse diffusion.

In this paragraph, we briefly explore its effect on the eigenproperties. Figure 8 panels *a* and *b* shows the behavior of $\Lambda_{\rm mp}$ in the presence of axial diffusion as a function of the Péclet number at two values of $\beta_{\rm ppm}=1, 10$, for $\alpha=5$ and $\alpha=20$. The value $\alpha=5$ corresponds to a rather extreme "wide-bore" mixing unit. In any case, as can be observed from the data depicted in Figure 8, axial-diffusion influences the dominant decay exponent solely for small values of α and for $\mathrm{Pe} \leq 10^2$. As the Péclet number increases its influence is completely immaterial on the behavior of the dominant decay exponent, and of the higher eigenmodes (not shown for the sake of brevity). This justifies the assumption of neglecting it, as enforced in the previous paragraphs.

Spectral analysis of diffusive mapping matrix

Let $\{\lambda_k, \boldsymbol{v}_k\}_{k=1}^N$ be the countable system of eigenvalues (λ_k) and eigenfunctions ($\boldsymbol{v}_k$) of $\boldsymbol{\Phi}$, $\boldsymbol{\Phi}\boldsymbol{v}_k=\lambda_k\boldsymbol{v}_k$. Due to the coarse-graining, the eigenvalues of the mapping matrix are influenced by numerical diffusion. This influence can be negligible if the Péclet number is at least one order of magnitude smaller than the mesh effective Péclet number $\mathrm{Pe}_{\rm eff}$, or can completely control diffusive processes for $\mathrm{Pe} \geq \mathrm{Pe}_{\rm eff}$.

The eigenvalues are bounded by $|\lambda_k| \leq 1$,[39,48] meaning that eigenmodes either decay exponentially in time ($|\lambda_k| < 1$) or persist indefinitely ($|\lambda_k|=1$). The eigenvalues of the mapping matrix can be ordered in such a way that $|\lambda_1| > |\lambda_2| \geq |\lambda_3| \geq \cdots \geq |\lambda_k| \geq \cdots$. The mapping matrix always possesses a nondegenerate real-valued persistent eigenmode with $|\lambda_1|=1$ due to mass conservation.[39,48] The persistent mode determines the asymptotic state $\boldsymbol{C}_\infty$ for $z \to \infty$. For the purely advective mapping matrix, for generic mesh structure, the eigenvalues λ_k with $k > 1$, gradually decline from unit modulus as the mode number k increases. This is a consequence of numerical diffusion, as all the eigenvalues of the continuum advection operator should possess a modulus strictly equal to 1. The concept of generic meshes should be briefly explained. The eigenvalues of the purely advective mapping matrix are for almost all the meshes strictly less than 1 in modulus, apart for specific subergodic partitions $\{\Omega_i\}_{i=1}^M$ (forming a subset of zero measure in the space of all the possible meshes) such that the union of a finite number of elements of $\{\Omega_i\}_{i=1}^M$ coincides with an invariant subset of the kinematics.

Decaying modes with $|\lambda_k| < 1$ determine the progression toward the asymptotic state. The contribution of each mode after n iterations, that is, at the outlet section of the n-th unit mixing modulus, is weighted by the decaying factor $|\lambda_k|^n$. After a transient, the progression toward the asymptotic state becomes dominated solely by the slowest-decaying eigenmode(s). Figure 9 illustrates the eigenvalue spectrum of the first 30 dominant eigenmodes for $\beta_{\rm ppm}=1$ panel *a* and $\beta_{\rm ppm}=10$ panel *b*. The values of $\lambda_k (k=1, \ldots, 30)$ were obtained from the diffusive mapping matrix at different Péclet numbers and from the purely advective matrix (corresponding to $\mathrm{Pe}=\mathrm{Pe}_{\rm eff}$).

Let us first consider the purely advective case (the eigenvalues are denoted by "○"). The difference $\Delta\lambda=|\lambda_2|-|\lambda_4| \sim 10^{-5}$ for $\beta_{\rm ppm}=1$ is negligibly small. The moduli of the eigenvalues from the second to the fourth $\lambda_k(k=2,3,4)$ are extremely close to each other. Therefore, the evolution of a scalar field (progression toward the asymptotic state) is primarily determined, in this case, by the first four modes.[48] The corresponding eigenvectors are localized at the major

Table 2. Prefactor p_0 vs. Parameter of the Flow $\beta_{\rm ppm}$

$\beta_{\rm ppm}$	1	4	8	10
p_0	33	40	20	60

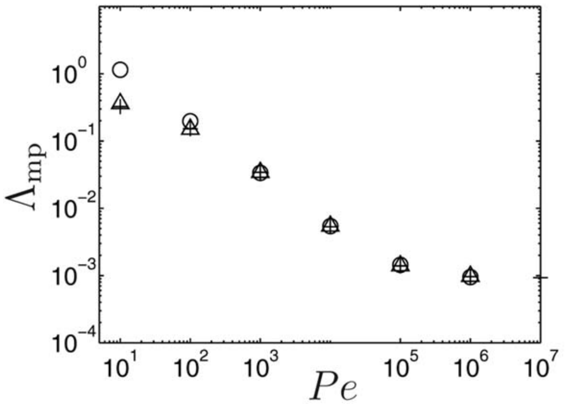

(a) (b)

Figure 8. Dominant decay exponent of the diffusive mapping matrix Λ_{mp} vs Pe_{eff} (markers "+") without axial diffusion.

Markers "△" correspond to Λ_{mp} including axial diffusion at $\alpha=20$; markers "○" at $\alpha=5$. Panel (*a*) corresponds to $\beta_{ppm}=1$ and panel (*b*) to $\beta_{ppm}=10$.

quasiperiodic islands, see Figure 12, and their spatial profiles are similar to Poincaré section depicted on Figure 3 panel *a*. For $\beta_{ppm}=10$, a similar tendency is also observed for the eigenvalues $\Delta\lambda=|\lambda_2|-|\lambda_4|\sim 10^{-4}$, as for structure of the corresponding eigenvectors $\mathbf{v}_k(k=2,3,4)$.

The inclusion of the molecular diffusion changes the spectral picture, especially as it regards the spectral gap between the first dominant eigenvalues. The difference $\Delta\lambda$ between second dominant eigenmode and the immediately subsequent ones increases significantly. For instance, at $Pe=10^3$ for $\beta_{ppm}=1$, the second and third eigenvalues $\{\lambda_2,\lambda_3\}$ form a complex conjugate pair with modulus $|\lambda_2|=0.9341$. The difference $\Delta\lambda$ with respect to the next following eigenmode λ_4 is $\Delta\lambda=|\lambda_2|-|\lambda_4|\approx 0.008$ and is considerably larger compared to purely advective mapping matrix. This means that for large n, the quantity $|\lambda_4|^n$ decays much faster along the axial coordinate, suppressing the influence of the fourth mode after few iterations. Therefore, after a very short transient, the role of all modes with index $k\geq 4$ becomes practically insignificant. For $\beta_{ppm}=10$, the situation is analogous, $\Delta\lambda=|\lambda_2|-|\lambda_4|\approx 0.076$ for $Pe=10^3$. Thus, decreasing Péclet number, the spectral gap, between the second (dominant) eigenmode and the higher ones becomes more pronounced. Eventually, asymptotic state is mainly determined by this single mode. For large Péclet numbers ($Pe\rightarrow\infty$), the decay toward the asymptotic homogeneous state is controlled by a set of dominant modes with eigenvalue moduli $|\lambda_k|$ extremely close to each other. The spatial structure of the corresponding

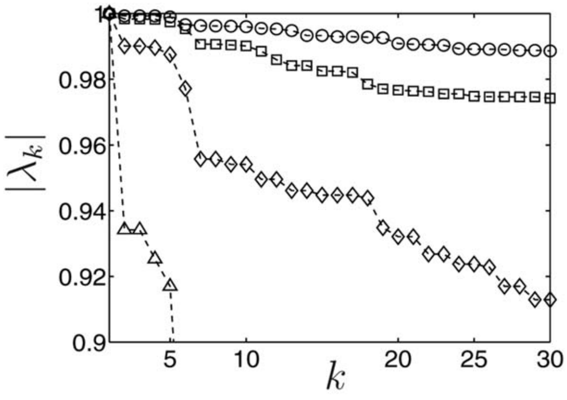

(a) (b)

Figure 9. Eigenvalue spectrum of the first 30 dominant eigenmodes associated with the PPM flow at different values of Péclet number.

Markers "○" correspond to $|\lambda_k|$ obtained from the purely advective mapping matrix ($Pe=Pe_{eff}$). Markers "□" refer to eigenvalues of the diffusive mapping matrix with $Pe=10^5$; "◇" to $Pe=10^4$; "△" to $Pe=10^3$. Panel (*a*) refers to $\beta_{ppm}=1$; panel (*b*) to $\beta_{ppm}=10$; The mesh structure used to generate the mapping matrices contains $N=31,776$ elements.

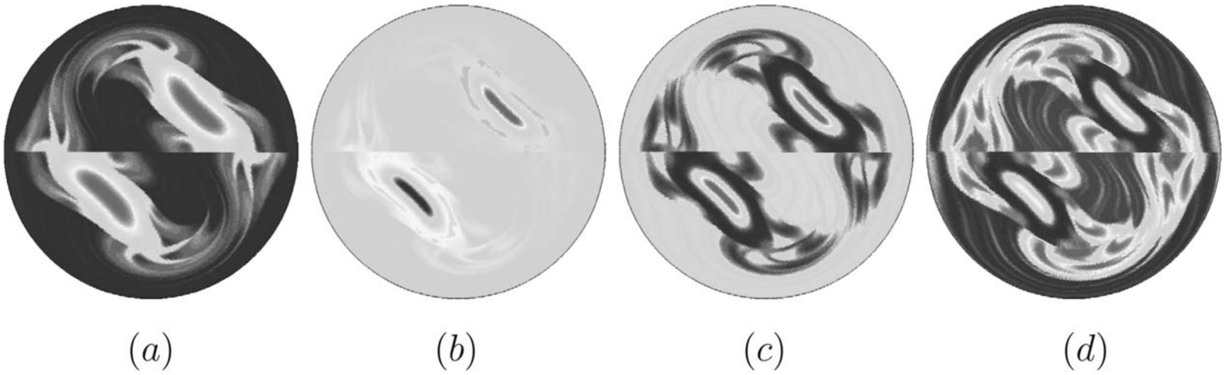

Figure 10. Dominant eigenvectors v_k of the diffusive mapping matrix for $\beta_{ppm} = 8$ at $Pe = 10^5$.

Panel (*a*) refers to v_2; panel (*b*) to v_3; panel (*c*) to v_4; and panel (*d*) to v_5. Green color corresponds to a zero value of v_k, red and blue to a maximum and minimum values, respectively.

eigenfunctions (all real-valued) for $k=2,3,4,5$ is depicted in Figures 10 and 11 for $\beta_{ppm}=8$ and $\beta_{ppm}=10$, respectively. As can be observed, all these eigenfunctions are localized at the main quasiperiodic regions of the corresponding Poincaré sections (see Figure 3 panels *d* and *e*), but the spatial profile of the eigenmodes develops also in the form of a filamentous, flamelet-like structure throughout the main chaotic region. This phenomenon is more pronounced for $\beta_{ppm}=10$, while can be observed at $\beta_{ppm}=10$ solely starting from the fifth eigenfunctions (being the previous ones almost exclusively localized at the four main quasiperiodic islands). The presence of these flamelet-like patterns is an indication of an active transport (material exchange) amongst the main regular subsets and the chaotic region that is still active for relatively high Péclet values (order of 10^5).

The eigenvalues in the diffusive case, especially for relatively high diffusivity, show a more pronounced and sudden drop from λ_1 to λ_2 (e.g., for $Pe=10^3$ the dominant eigenvalue equals $\lambda_2=0.9341$ for $\beta_{ppm}=1$) and this leads to better mixing performance.[48] This phenomenon is a direct consequence of the changes in the eigenmodes properties. Figures 12 and 13 illustrate these properties, and how the eigenmode structure changes as a function of the Péclet number. For a better illustration, typical eigenfunctions in the range $k \in [2,50]$ are selected. For each eigenmodes (the value of k is indicated below) symbol R stands for real-valued eigenfunctions, while R^* indicates that eigenfunction multiplicity occurs: eigenvalue/eigenfunction arises as a complex conjugate pair, and the real part is illustrated. In order to follow the connection between invariant regions of the Poincaré section and eigenmode structures, eigenmodes at different value of the modal number k should be compared.

Figure 12 depicts the typical structures of the dominant eigenvectors $\mathbf{v}_k$ (in the range $k \in [2,50]$) for the PPM flow at $\beta_{ppm}=1$. The first dominant/persistant eigenmodes (with $|\lambda_k|$ closest to the unity) typically correspond to the major invariant quasiperiodic islands. This tendency characterizes the behavior of the advection–diffusion operator starting from relatively small values of Pe (order of 10^3), see Figure 12 panel *a*. In the purely advective case, when diffusive contribution arise purely due to the coarse-graining with corresponding $Pe=Pe_{eff}$, the spatial structure of the transient eigenmodes is consistent with that of the Poincaré section,[48] see Figure 12. The structure of small-scale regular islands observed on the Poincaré sections accurately superimposes on the regions where the eigenmodes are mainly localized (Figure 12, advection, panels *c*–*d*). Decreasing the Péclet number, transient eigenmodes for small-scale regular zones gradually degenerate to more complex patterns, as clearly illustrated in Figure 12 panel *d* and in Figure 13.

In the range $k=[2,50]$, these eigenmodes degenerate into spatial structures which are distributed exchange zones

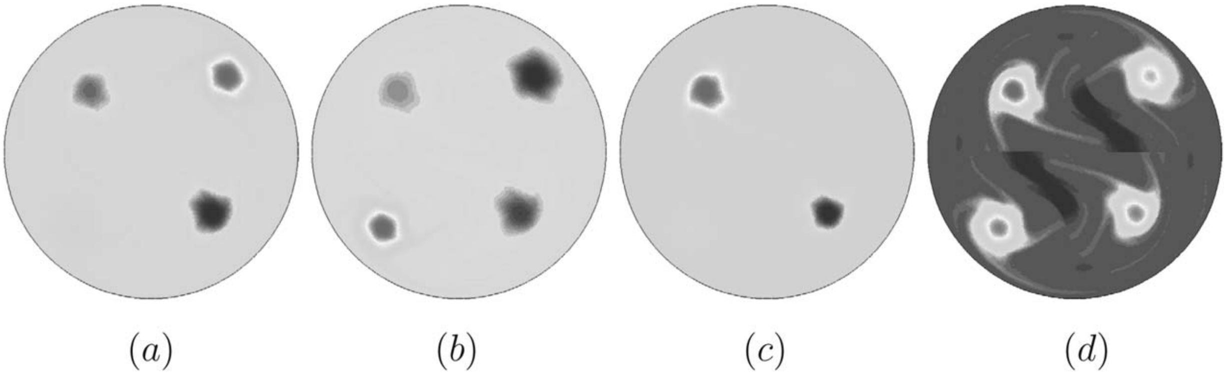

Figure 11. Dominant eigenvectors v_k of the diffusive mapping matrix for $\beta_{ppm} = 10$ at $Pe = 10^5$.

Panel (*a*) refers to v_2; panel (*b*) to v_3; panel (*c*) to v_4; and panel (*d*) to v_5.

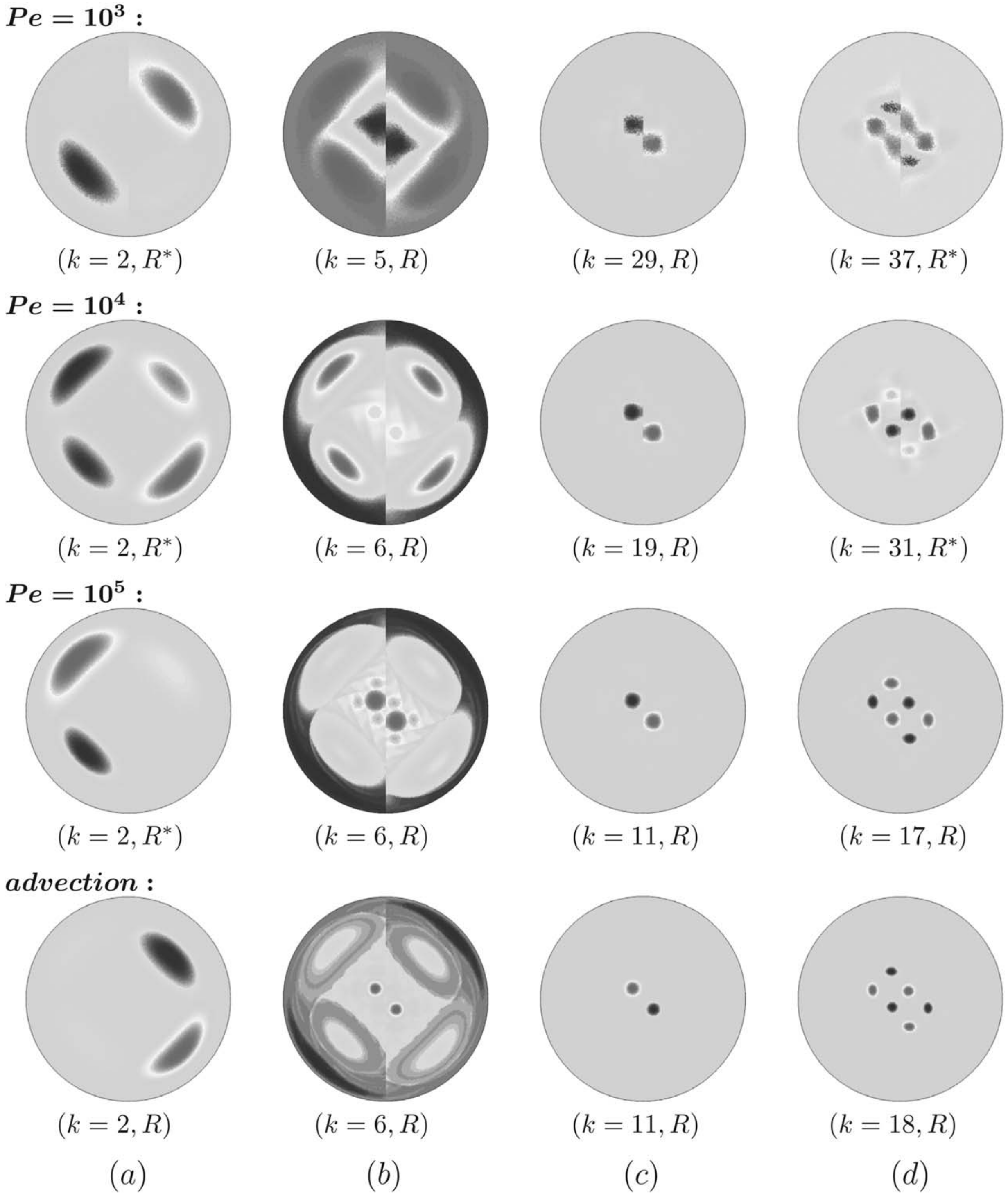

Figure 12. Typical eigenvectors v_k ($k=2,30$) of the mapping matrix for $\beta_{ppm}=1$ at several values of the Péclet number $Pe \in [10^3, 10^5]$ and in the purely advective case ($Pe = Pe_{eff}$).

amongst the chaotic regions and large-scale regular islands. Figure 12 panel *c* shows a partial degeneration of the mode, the corresponding eigenvector is localized onto two symmetric medium size islands in the center of the domain. Increasing the influence of diffusion, the boundaries of the islands gradually diffuse and grow in size, although general structure is preserved.

The pictorial illustration of eigenmodes degeneration and how it depends on the Péclet number is depicted in Figure 13 for $\beta_{\text{ppm}} = 1, 10, 20$. The case $\beta_{\text{ppm}} = 10$, similarly to $\beta_{\text{ppm}} = 1$, is characterized by the existence of regular islands with different sizes. Small-scale regions are represented by two pairs of quasiperiodic island. Particularly interesting is the influence of diffusion on the transient eigenmodes that correspond to these invariant regions. In the purely advective case patterns of small-scale islands, where the eigenmodes are localized, clearly match the corresponding invariant structures of the Poincaré sections, see Figure 13 panel *d*.

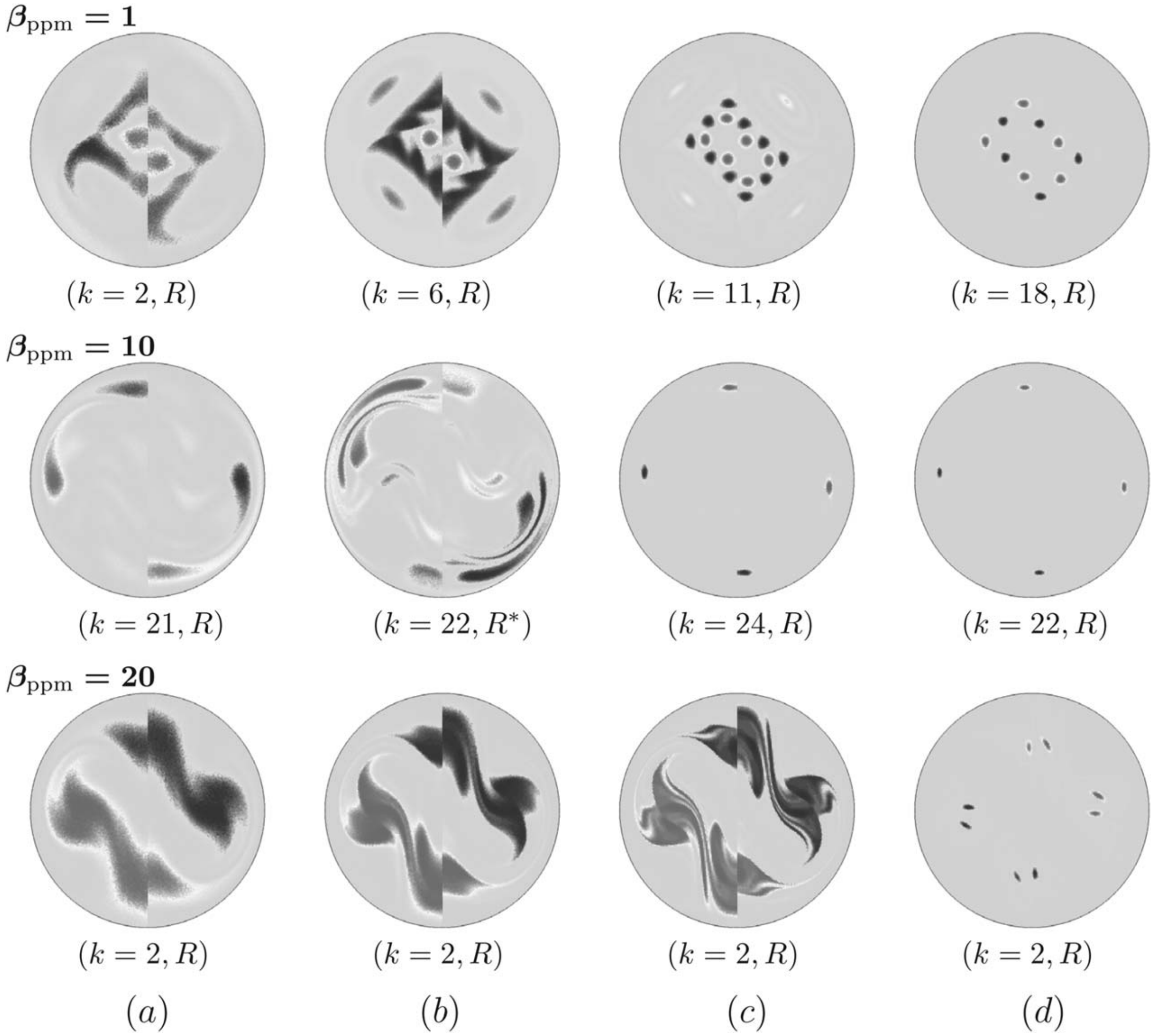

Figure 13. Typical eigenvectors of the mapping matrix, in the range (k=2, 50), for different values of β_{ppm} at several values of the Péclet number: panel (a)Pe =10^3; panel (b)Pe =10^4; panel (c)Pe =10^5; panel (d) purely advective case (Pe =Pe$_{\mathrm{eff}}$).

The inclusion of the diffusion leads to a degeneration of these structures as discussed for $\beta_{\mathrm{ppm}} = 1$. Eigenvectors of transient eigenmodes degenerate into more complicated structures that involve the overlapping of other regular zones with the main chaotic region, see panels *a* and *b*.

The Poincaré section for $\beta_{\mathrm{ppm}} = 20$ reveals the existence of eight small-scale regular periodic islands, and their structure reflects into localization patterns of some of the dominant eigenmodes for high Péclet numbers.[38,39,48] Figure 13 panel *d* shows the second dominant eigenmode for $\beta_{\mathrm{ppm}} = 20$. This case corresponds to a gradual degeneration of the spatial invariant pattern. Such behavior can be also observed as a function of β_{ppm}. The parameter β_{ppm} is proportional to the length of periodic unit. Consequently, for constant axial velocity, by increasing β_{ppm} the characteristic time needed for particle to reach the outlet section of the mixing unit also increases. This fact explains the influence of β_{ppm} on the degeneration of the spatial patterns of the eigenmodes. For $\beta_{\mathrm{ppm}} = 20$, the degeneration of small-scale islands occurs even for Pe $= 10^5$, see Figure 13, as opposed to the case $\beta_{\mathrm{ppm}} = 1$ when even at Pe $= 10^3$ the structure of small-scale invariant islands can be still observed.

Comparative analysis of the spatial structures of the dominant eigenvectors obtained by the mapping method and analysis of the advective-diffusive operator shows a good agreement. However, such analysis is out of the scope of the present article.

To sum up, the spectral analysis of the diffusive mapping matrix is an efficient tool for investigating the fine structures associated with advective-diffusive transport. It reveals the detailed properties of the distributive mixing, and the patterns arising a consequence of the exchange between different kinematic invariant regions. Ultimately, all relevant information is stored in the eigenmodes, and the analysis of their spatial patterns, and especially of the influence of the Péclet number on their profile, is a valid alternative to the "frozen" picture arising from the analysis of the kinematic Poincaré sections.

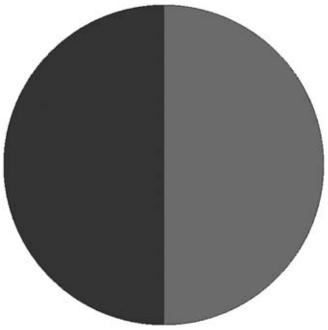

Figure 14. Initial distribution of concentration at the inlet cross section of the PPM.

In this sense, the analysis of the eigenmodes provides a powerful and efficient approach that provides all detailed information about the existence of regular zones, their interaction as a function of the intensity of the diffusive transport, and their distribution in the flow domain.

Advective-Diffusive Transport: Concentration Evolution

As discussed in the previous sections, the diffusive mapping-matrix approach is a computationally powerful and quantitatively reliable method for investigating advection–diffusion processes. In this section, we analyze the spatial evolution of the concentration field for different values of the Péclet number and flow protocols. As discussed in previous paragraph, the impact of diffusion along the axial direction is practically negligible with respect to transverse diffusion in all the cases of practical interest.

As initial (inlet) condition, we consider a segregated concentration distribution with $C_{0,i}=0$ for the elements Ω_i for which the corresponding abscissa x_i lies in the interval $-1 \leq x_i \leq 0$, and $C_{0,1}=1$ for $0 < x_i \leq 1$, see Figure 14. The simulations refer to a mesh with linear size $\Delta x=0.005$, containing 281,442 elements.

Static mixers of engineering practice consist of a finite number of units. Consequently, the analysis of the mixing process for small values of n is also relevant in the applications. Figure 15 shows the evolution of the inlet state (Figure 14) over the first 10 units for $\beta_{\mathrm{ppm}}=1$. We consider advective-diffusive mixing modeled by the diffusive mapping matrix at several Péclet number ($\mathrm{Pe}=10^3, 10^4, 10^5$) and compare them with the simulations obtained by the purely advective mapping matrix, the effective Péclet number of which is above 10^6.

At $\beta_{\mathrm{ppm}}=1$, invariant regular islands of quasiperiodic motion of different sizes, are distributed all over the cross-section of the mixer, see Figure 3 panel *a*. As discussed above, the material exchange between different invariant islands of quasiperiodicity can occur solely by diffusion. For the chosen initial conditions, see Figure 14, regular islands are filled by fluid at uniform solute concentration. First, consider the purely advective mapping matrix, for which coarse-graining acts as a superimposed diffusive contribution, corresponding $\mathrm{Pe}_{\mathrm{eff}} \approx 1.3\times10^6$. After 10 periods of mixing, the concentration profile resembles closely the spatial structure of the corresponding Poincaré section, see Figure 15 panel *d*.

Variation of the Péclet numbers results in considerable changes of the mixing patterns. Decreasing Pe, rapid diffusion of the small-scale islands occurs. At $\mathrm{Pe}=10^4$ (panel *b*) after 10 period, the system of small-scale islands located in the center of the domain is almost completely destroyed. At $\mathrm{Pe}=10^3$ (panel *a*), the central region becomes uniformly mixed after 10 period. At the same time, the boundaries of the major islands shrink in size, leading to a more efficient homogenization process.

A similar situation is observed for the other values of the control parameter β_{ppm}. Evolution of the concentration field starting from the same inlet condition at $\beta_{\mathrm{ppm}}=8$ and $\beta_{\mathrm{ppm}}=10$ is illustrated in Figures 16 and 17, respectively.

The quantification of the homogenization performance can be obtained by using the discrete intensity of segregation. Figure 18, panels *a–c* illustrates the dependence of the intensity of segregation I_{d} on the number of units n for several values of β_{ppm} and Pe.

The intensity of segregation I_{d} is a measure of the deviation of the local concentration from the perfectly mixed condition, which represents a homogeneous state of the mixture. Decrease of the Péclet number, in all cases of parameter β_{ppm}, leads to faster decay of I_{d} along the axial coordinate and consequently to better mixing performance. This shows, if still necessary, the importance of including the effect of molecular diffusion in the simulation and optimization of mixing processes. As can be observed from the data reported in Figure 18 panels *b* and *c*, the decay rate of I_{d} as a function of the number n of the mixing unit, for fixed Pe is much higher for $\beta_{\mathrm{ppm}}=8$, and $\beta_{\mathrm{ppm}}=10$ than for $\beta_{\mathrm{ppm}}=1$. This is not surprising, as the parameter β_{ppm} is proportional to the length $2L$ of the mixing unit, and consequently is proportional to the characteristic travelling time $\Delta\tau$ for a fluid particle to pass the unit of the mixer. The effect of the diffusion becomes more pronounced as $\Delta\tau$ increases (simply as a consequence of the Einstein's relation[41]).

Conclusions

This article has proposed the extension of the mapping matrix approach to include the effect of molecular diffusion in the analysis of open-flow devices and static mixers.

The way the inlet/outlet mapping matrix is constructed is essentially Lagrangian, but it enforces a stochastic differential equation (Langevin equation) for fluid particle motion, in which diffusion enters as a stochastic contribution. This way of generating diffusive matrices admits several significant advantages, especially when applied to realistic mixing devices characterized by a complex internal geometry and by nontrivial flow fields. The main advantage is that it provide an Eulerian (albeit coarse-grained) description of the interaction between advection and diffusion, and ultimately of the mixing process, by solely solving a stochastic Lagrangian kinematics for the advecting-diffusing particles, in which the effects of any complex geometry of the device impacts solely on the implementation of the reflecting boundary conditions at the solid boundaries of the mixing unit.

Therefore, the analysis developed in the present article for the PPM applies as is, without modifications or extra computational efforts to any other model of a realistic static mixer.

The approach proposed is suited for describing, steady and unsteady conditions, and to include if necessary the effect of

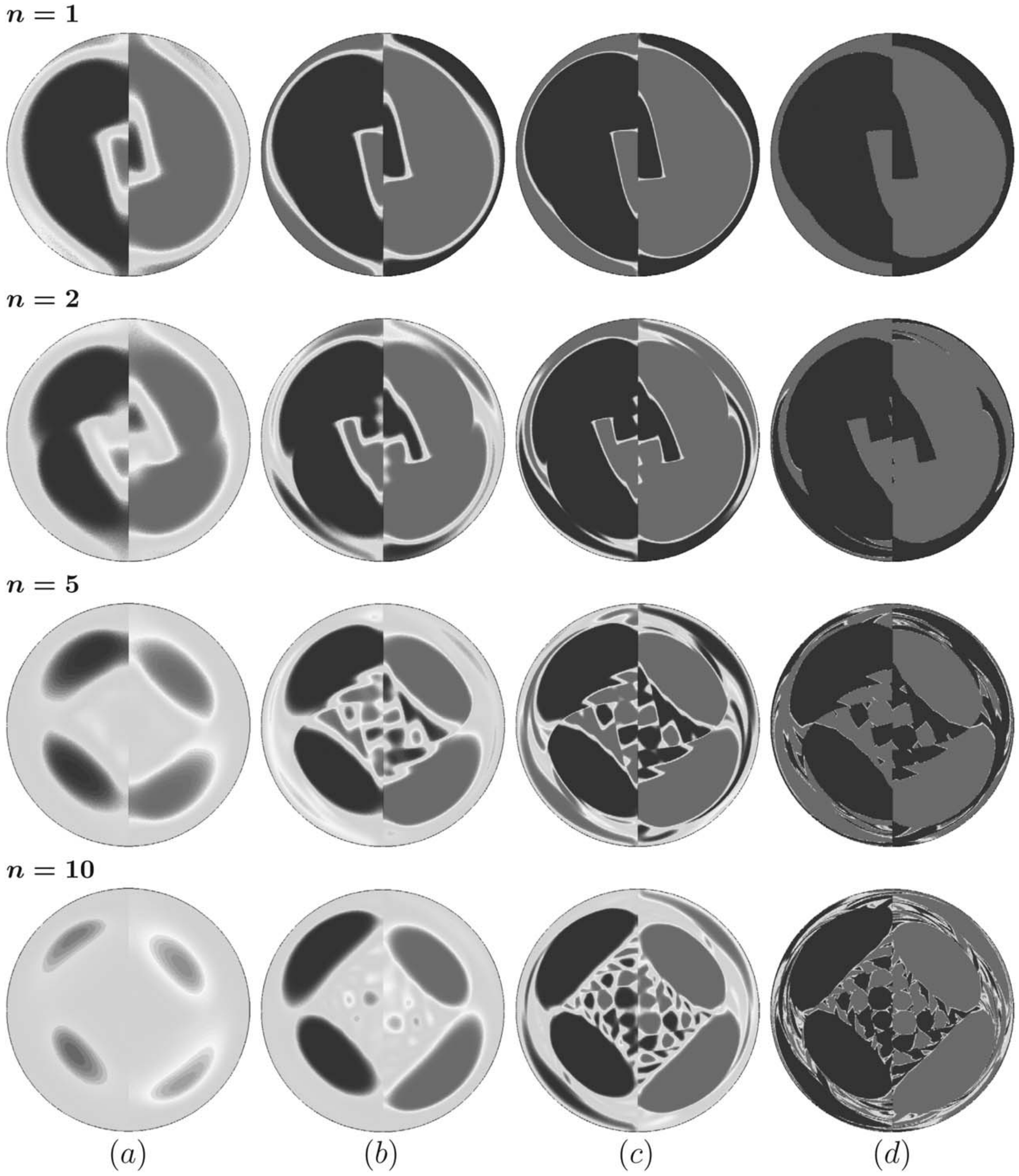

Figure 15. Distribution of concentration in the PPM for $\beta_{\mathrm{ppm}} = 1$ after $n = 1, 2, 5, 10$ periods.

Panel (*a*) depicts the evolution of mixing patterns for advective-diffusive mixing at $\mathrm{Pe} = 10^3$; panel (*b*) at $\mathrm{Pe} = 10^4$; panel (*c*) at $\mathrm{Pe} = 10^5$. Panel (*d*) corresponds to the purely advective case. The mesh contains 281,442 elements and the effective Péclet number equals $\mathrm{Pe}_{\mathrm{eff}} \approx 1.3 \times 10^6$.

axial diffusion. However, in practical mixing equipment for $\mathrm{Pe} > 10^2$ and realistic aspect ratios, the effect of axial diffusion is completely negligible.

One of the main byproduct of the present analysis of the diffusive mapping matrix is the fact that this approach has recast the purely advective mapping method in a new light, namely as a reliable approximation for advective-diffusive transport, due to the effect of numerical diffusion. An often undesired effect, such numerical diffusion, here is enforced in a coarse-grained formulation of pure advection, just to mimic, in a reliable and quantitative way, the more realistic advection–diffusion process. This is made possible due to the concept of the effective Péclet number and of its simple dependence on the mesh resolution.

Numerical results (see Figure 5) have shown that the dominant decay exponent deriving from purely advective

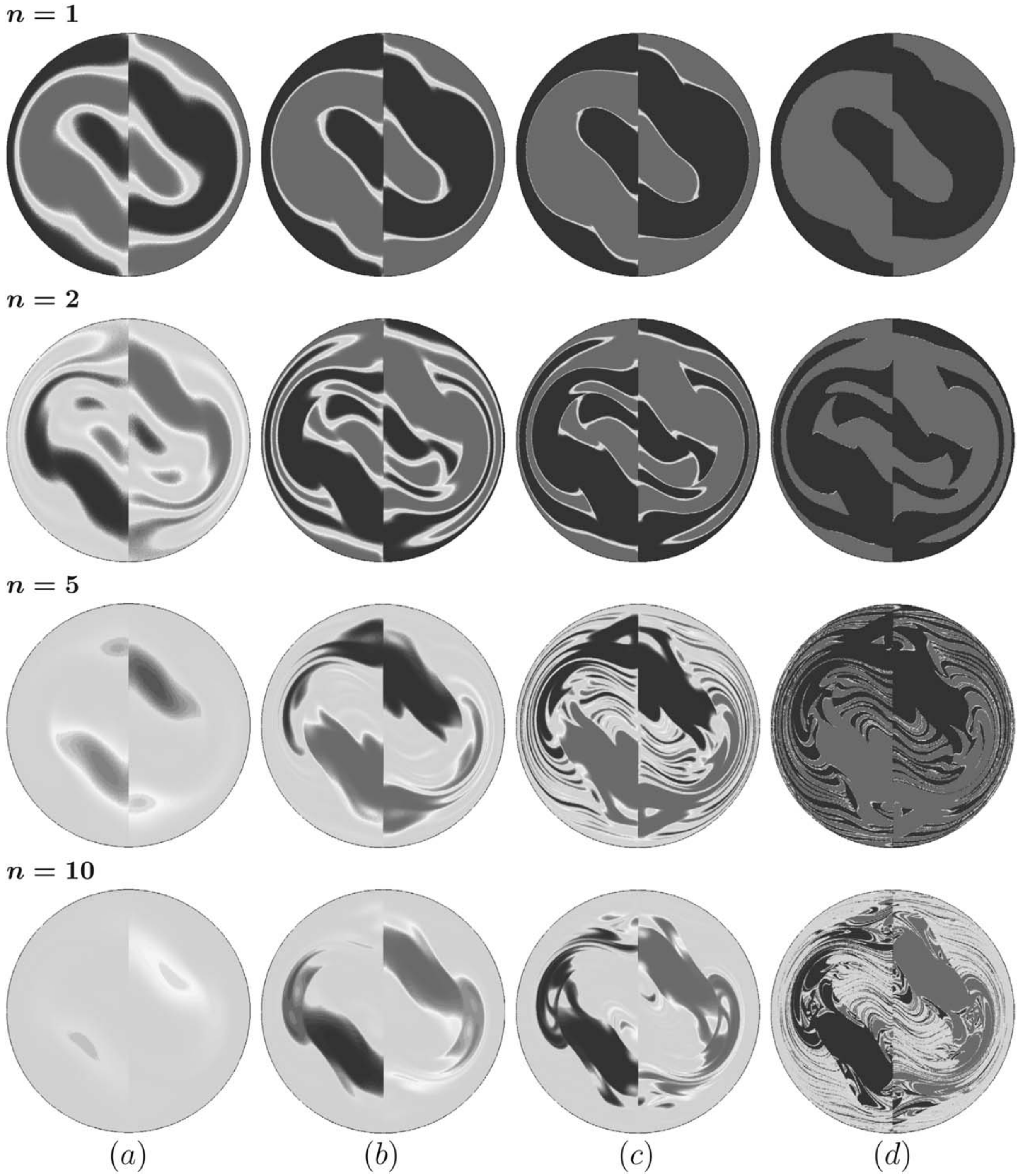

Figure 16. Distribution of concentration in the PPM for $\beta_{\mathrm{ppm}}=8$ after $n=1,2,5,10$ periods.

Panel (*a*) depicts the evolution of mixing patterns for advective-diffusive mixing at Pe $=10^3$; panel (*b*) at Pe $=10^4$; panel (*c*) at Pe $=10^5$. Panel (*d*) corresponds to the purely advective case (for the mesh used, containing 281,442 elements, Pe$_{\mathrm{eff}}\approx 10^6$).

mapping simulations and its eigenfunctions (as well as for higher-order modes, Figure 6) provide an accurate estimate of the corresponding quantities associated with the continuum advection–diffusion operator at a value of the Péclet number equal to the effective Péclet number of the mesh.

In this way, it is possible to simulate mixing process at extremely high values of Pe (Pe $\simeq 10^7-10^9$), just increasing mesh resolution and performing purely advective (nonstochastic) kinematics. This is a major practical result compared to the existing numerical methods (finite elements, finite volumes, or Galerkin expansions), the range of validity of which in mixing analysis over realistic computational structures hardly exceed Pe $=10^6$.

We have thoroughly discussed the spatial structure of the eigenmodes and their relation with the main kinematic invariant sets (quasiperiodic islands) that characterize the Poincaré section of the kinematic (diffusionless) equation of motion. In point of fact, from the structure of the dominant eigenfunctions and of the higher-order modes, coupled with the estimate of their mutual spectral gaps, it is possible to achieve a very

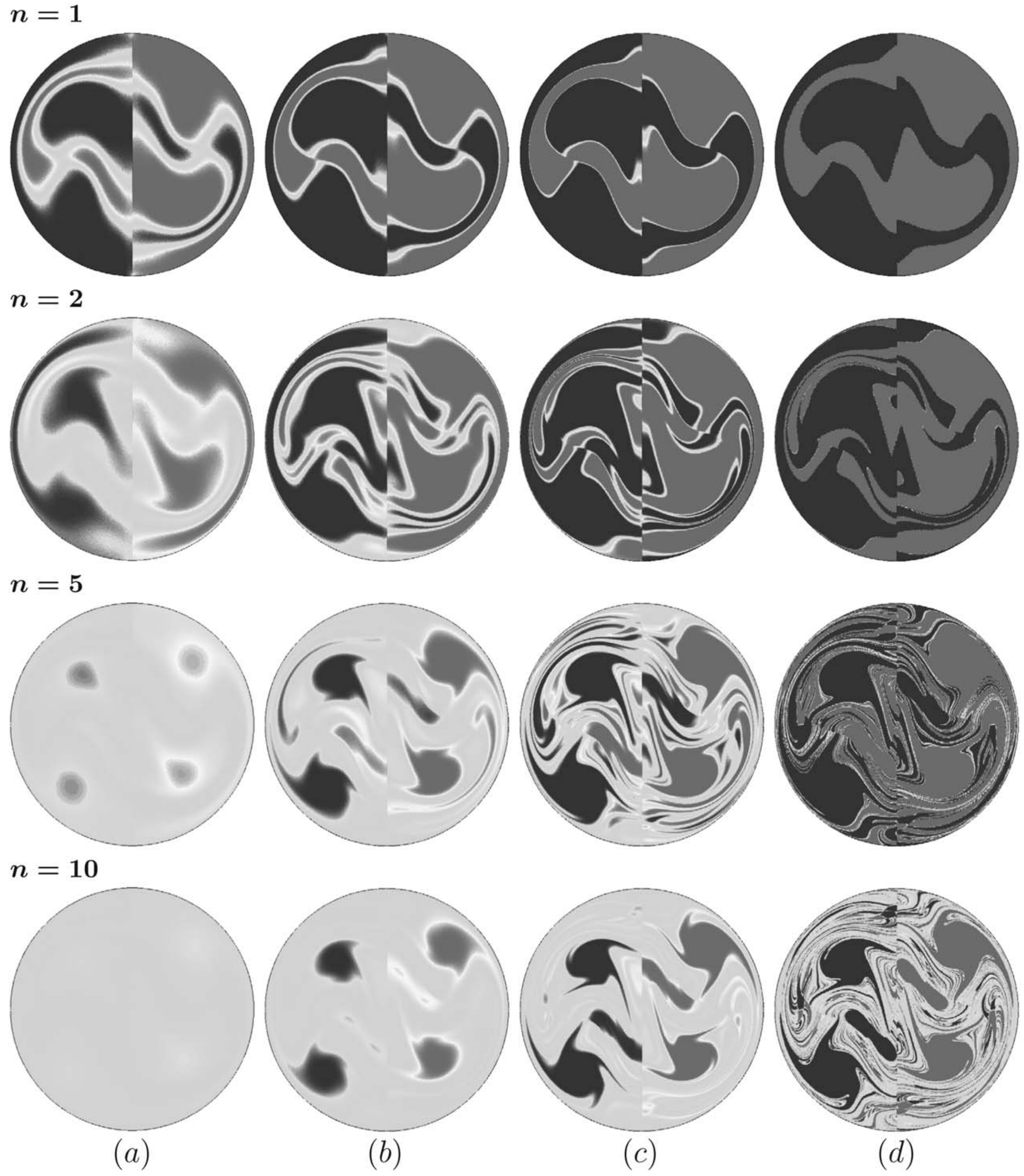

Figure 17. Distribution of concentration in the PPM for $\beta_{\text{ppm}} = 10$ after $n = 1, 2, 5, 10$ periods.

Panel (*a*) depicts the evolution of mixing patterns for advective-diffusive mixing at $\text{Pe} = 10^3$; panel (*b*) at $\text{Pe} = 10^4$; panel (*c*) at $\text{Pe} = 10^5$. Panel (*d*) corresponds to the purely advective case ($\text{Pe}_{\text{eff}} \approx 2\times10^6$).

detailed qualitative understanding of the of a mixing process and of the geometry of the resulting partially mixed structures. This qualitative picture, deriving from the analysis of the eigenfunction profiles, is in some sense more general, and physically more significant, than the inspection of the pure diffusionless Poincaré section. The actual generation of scientists and engineers in the field of laminar chaotic mixing has grown with the kinematic paradigm based on Poincaré sections, Lyapunov exponents and so forth.[9] This paradigm is a part of a bigger paradigm in which diffusion enters, made by eigenfunctions and eigenvalues of transport operators, on which probably the next generation will grow up. The extended mapping matrix and its implications (such as the use of the purely advective mapping matrix as an advection–diffusion emulator) makes this new paradigm simple and computationally efficient to use.

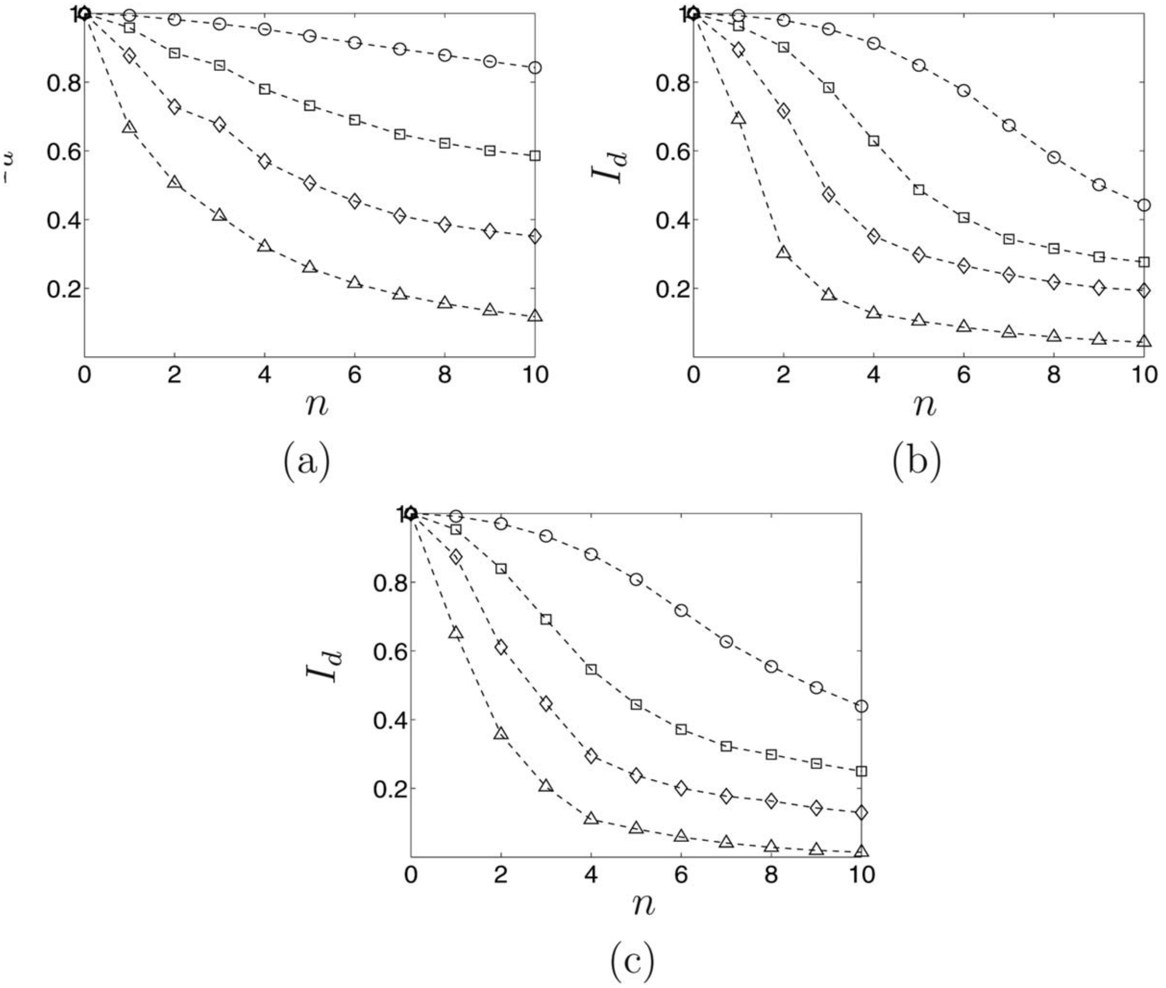

(a) (b)

(c)

Figure 18. Dependence of the intensity of segregation I_d on the number of mixing units *n*.

Markers "○" refer to the purely advective mapping matrix, "□" correspond to advective-diffusive mixing at Pe $=10^5$; "◇" at Pe $=10^4$; "△" at Pe $=10^3$. Panel (*a*) refers to $\beta_\mathrm{ppm}=1$; panel (*b*) to $\beta_\mathrm{ppm}=8$; panel (*c*) to $\beta_\mathrm{ppm}=10$.

Notation

$\mathbf{\Phi}, \mathbf{\Phi}_{ij}$ = mapping matrix, entries of the mapping matrix
λ_k, $\mathbf{v}_k$ = Eigenvalues/eigenvectors of the mapping matrix
Λ = dominant decay exponent of the advection–diffusion operator, see Eq. 10
$\Lambda_\mathrm{mp}, \Lambda^c_\mathrm{mp}$ = dominant decay exponent of the diffusive/advective mapping matrix
β = exponent expressing the power-law scaling of the dominant eigenvalue
c = concentration field
$\boldsymbol{C}_n$ = concentration vector after n periods
Pe, Pe_eff = Péclet number, effective Péclet number
Δx = linear size of the element in the mesh
$N_c=1/\Delta x$ = value inversely proportional to Δx
N_p = number of particles in the cell of the mesh
p_0 = Prefactor
β_ppm = control parameter of PPM
t = time
T_p = period of the flow
$\mathbf{v}$ = velocity field
$\mathbf{x}_\perp, z$ = transverse and axial coordinate
$\mathbf{v}_\perp, w$ = transverse and axial velocity
$\boldsymbol{\xi}$ = vector-valued stochastic process
$\mathbf{r}_n$ = realization of normally distributed independent random variable
Σ_T = transverse cross-section of the mixing device
P = probability density function
I_d = intensity of segregation
h = time step in Euler-Langevin scheme
R, L = sizes of PPM
r, θ = polar coordinates
Ω_i = cell in the mesh
N = number of cells in the mesh
N_F = truncation order of the Fourier expansion

Literature Cited

1. Cortelezzi L, Mezić I, editors. *Analysis and Control of Mixing with an Application to Micro and Macro Flow Processes*. Wien: Springer, 2009.
2. Harnby N, Edwards MF, Nienow AW. *Mixing in the Process Industries*. Oxford: Butterworth-Heinemann, 1992.
3. Thakur RK, Vial C, Nigam KDP, Nauman EB, Djelveh G. Static mixers in the process industries—a review. *Chem Eng Res Des.* 2003;81:787–826.
4. Baldyga J, Bourne JR. *Turbulent Mixing and Chemical Reactions*. New York: Wiley, 1999.
5. Baird DG, Collias DI. *Polymer Processing Principles and Design*. New York: Wiley, 1998.
6. Kukura J, Arratia PC, Szalai ES. Understanding pharmaceutical flows. *Pharm Technol.* 2002;26:48–60.
7. Alvarez MM, Zalc JM, Shinbrot T, Arratia PE, Muzzio FJ. Mechanisms of mixing and creation of structure in laminar stirred tanks. *AIChE J.* 2002;48:2135–2148.
8. Childress S, Gilbert AD. *Stretch, Twist and Fold: The Fast Dynamo*. Berlin: Springer-Verlag, 1995.
9. Ottino JM. *The Kinematics of Mixing: Stretching, Chaos, and Transport*. Cambridge: Cambridge University Press, 1989.
10. Aref H. Stirring by chaotic advection. *J Fluid Mech.* 1984;143:1–21.
11. Zalc JM, Szalai ES, Alvarez MM, Muzzio FJ. Using cfd to understand chaotic mixing in laminar stirred tanks. *AIChE J.* 2002;48:2124–2134.

12. Solomon TH, Mezić I. Uniform resonant chaotic mixing in fluid flows. *Nature*. 2003;425:376–380.
13. Cerbelli S, Adrover A, Creta F, Giona M. Foundations of laminar chaotic mixing and spectral theory of linear operators. *Chem Eng Sci*. 2006;61:2754–2761.
14. Alvarez MM, Muzzio FJ, Cerbelli S, Adrover A, Giona M. Self-similar spatiotemporal structure of intermaterial boundaries in chaotic flows. *Phys Rev Lett*. 1998;81:3395–3398.
15. Muzzio FJ, Alvarez MM, Cerbelli S, Giona M, Adrover A. The intermaterial area density generated by time- and spatially periodic 2d chaotic flows. *Chem Eng Sci*. 2000;55:1497–1508.
16. Pauline D, Tanguy PA, Le Blevec J-M, Bousquet J. Numerical investigatigation of the performance of several static mixers. *Can J Chem Eng*. 1998;76:527–535.
17. Zalc JM, Szalai ES, Muzzio FJ, Jaffer S. Characterization of flow and mixing in an smx static mixer. *AIChE J*. 2002;58:427–436.
18. Adrover A, Cerbelli S, Giona M. A spectral approach to reaction/diffusion kinetics in chaotic flows. *Comput Chem Eng*. 2002;26:125–139.
19. Singh MK, Anderson PD, Meijer HEH. Understanding and optimizing the smx static mixer. *Macromol Rapid Commun*. 2009;30:362–376.
20. Spencer R, Wiley R. The mixing of very viscous liquids. *J Colloid Sci*. 1951;6:133–145.
21. Kruijt PGM, Galaktionov OS, Anderson PD, Peters GWM, Meijer HEH. Analyzing mixing in periodic flows by distribution matrices: mapping method. *AIChE J*. 2001;47(5):1005–1015.
22. Kang TG, Singh MK, Kwon TH, Anderson PD. Chaotic mixing using periodic and aperiodic sequences of mixing protocols in a micromixer. *Microfluid Nanofluid*. 2008;4:589–599.
23. Singh MK, Kang TG, Meijer HEH, Anderson PD. The mapping method as a toolbox to analyze, design and optimize micromixers. *Microfluid Nanofluid*. 2008;5:313–325.
24. Galaktionov OS, Anderson PD, Peters GWM, Meijer HEH. Morphology development in kenics static mixers (application of the extended mapping method). *Can J Chem Eng*. 2002;80:604–613.
25. Galaktionov OS, Anderson PD, Peters GWM, Meijer HEH. Analysis and optimization of kenics mixers. *Int Polym Process*. 2003; XVIII(2):138–150.
26. Meijer HEH, Singh MK, Kang TG, den Toonder JMJ, Anderson PD. Passive and active mixing in microfluidic devices. *Macromol Symp*. 2009;279(1):201–209.
27. Schijndel Tv, Singh MK, Gillies M, Kahya N, Kharin A, den Toonder JMJ. Toward gradient formation in microfluidic devices by using slanted ridges. *Macromol Mater Eng*. 2011;296:373–379.
28. Gorodetskyi O, Giona M, Anderson PD. Spectral analysis of mixing in chaotic flows via the mapping matrix formalism—inclusion of molecular diffusion and quantitative eigenvalue estimate in the purely convective limit. *Phys Fluids*. 2012;24:073603.
29. Gorodetskyi O, Giona M, Anderson PD. Exploiting numerical diffusion to study transport and chaotic mixing for extremely large péclet values. *Europhys Lett*. 2012;97:14002.
30. Popovych OV, Pikovsky A, Eckhardt B. Abnormal mixing of passive scalars in chaotic flows. *Phys Rev E*. 2007;75:036308.
31. Pierrehumbert RT. Tracer microstructure in the large-eddy dominated regime. *Chaos Solitons Fractals*. 1994;4(6):774–782.
32. Rothstein D, Henry E, Gollub JP. Persistent patterns in transient chaotic fluid mixing. *Nature (London)*. 1999;401:770–772.
33. Voth GA, Saint TC, Dobler G, Gollub JP. Mixing rates and symmetry breaking in two-dimensional chaotic flow. *Phys Fluids*. 2003; 15(9):2560.
34. Liu W, Haller G. Strange eigenmodes and decay of variance in the mixing of diffusive tracers. *Physica D*. 2004;188:1–39.
35. Lester DR, Rudman M, Metcalfe G, Blackburn HM. Global parametric solutions of scalar transport. *J Comput Phys*. 2008;227(6):3032–3057.
36. Sukhatme J, Pierrehumbert RT. Decay of passive scalars under the action of single scale smooth velocity fields in bounded two-dimensional domains: from non-self-similar probability distribution functions to self-similar eigenmodes. *Chaos Solitons Fractals*. 2002; 66:056302.
37. Giona M, Cerbelli S, Vitacolonna V. Universality and imaginary potentials in advection-diffusion equations in closed flows. *J Fluid Mech*. 2004;513:221–237.
38. Cerbelli S, Vitacolonna V, Adrover A, Giona M. Eigenvalue-eigenfunction analysis of infinitely fast reactions and micromixing regimes in regular and chaotic bounded flows. *Chem Eng Sci*. 2004;59:2125–2144.
39. Singh MK, Speetjens MFM, Anderson PD. Eigenmode analysis of scalar transport in distributive mixing. *Phys Fluids*. 2009;21:093601.
40. Liu M, Muzzio FJ, Peskin RL. Quantification of mixing in aperiodic chaotic flows. *Chaos Solitons Fractals*. 1994;4(6):869–893.
41. Chandrasekhar S. Stochastic problems in physics and astronomy. *Rev Mod Phys*. 1943;15:1–89.
42. Lasota A, Mackey MC. *Chaos, Fractals, and Noise: Stochastic Aspects of Dynamics*. Berlin: Springer-Verlag, 1994.
43. Kloeden PE, Platen E. *Numerical Solution of Stochastic Differential Equations*. Berlin: Springer Verlag, 1995.
44. Khakhar DV, Franjione JG, Ottino JM. A case study of chaotic mixing in deterministic flows: the partitioned-pipe mixer. *Chem Eng Sci*. 1987;42(12):2909–2926.
45. Hobbs DM, Swanson PD, Muzzio FJ. Numerical characterization of low reynolds number flow in the kenics static mixer. *Chem Eng Sci*. 1998;53:1565–1584.
46. Hobbs DM, Muzzio FJ. Optimization of a static mixer using dynamical systems techniques. *Chem Eng Sci*. 1998;53:3199–3213.
47. Singh MK, Galaktionov OS, Meijer HEH, Anderson PD. A simplified approach to compute distribution matrices for the mapping method. *Comput Chem Eng*. 2009;33:1354–1362.
48. Gorodetskyi O, Speetjens MFM, Anderson PD. An efficient approach for eigenmode analysis of transient distributive mixing by the mapping method. *Phys Fluids*. 2012;24(5):053602.

Appendix

Fourier Analysis of the Advection–Diffusion Equation in the PPM

This Appendix addresses briefly the Fourier analysis leading to the Galerkin expansion of the advection–diffusion equation in the PPM for negligible axial diffusion.

The PPM unit is made by two moduli, the second of which is just a rotation of the first by $\pi/2$. Consider the first half-modulus. Due to the presence of a solid wall at $\theta=\pi$, it is convenient to define a vector-valued concentration field $\mathbf{c}(\mathbf{x})$ for the upper (U) and lower (D) parts of the unit (see Figure A1, panel *a*)

$$\mathbf{c}(r,\theta,z)=\begin{pmatrix} c^U(r,\theta,z) \\ c^D(r,\theta,z) \end{pmatrix} \begin{matrix} c^U \text{for}\,\theta\in[0,\pi) \\ c^D \text{for}\,\theta\in[\pi,2\pi) \end{matrix} \tag{A1}$$

where $r\in[0,1)$ and $\theta\in[0,2\pi)$ are the polar coordinates describing the cross-section Σ_T. The fields $c^\alpha(r,\theta,z), \alpha=U,D$ can be expressed in Fourier series

$$c^\alpha(r,\theta,z)=\sum_{m,n=0}^{N_\mathrm{F}} c^\alpha_{m,n}(z)\cos(m\pi r)\cos(n\theta), \tag{A2}$$

where N_F is the truncation order in the Fourier expansion. These two fields satisfy the advection–diffusion equation

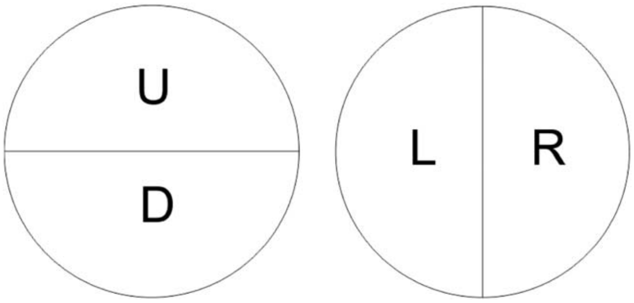

Figure A1. Representation of the fields c^U, c^L, c^R, c^L in the two half-moduli of the PPM.

$$r^2 w(r,\theta)\frac{}{\partial c^\alpha \partial z} = -\beta_{\text{ppm}}\, r^2 \hat{v}_r(r,\theta)\frac{\partial c^\alpha}{\partial r} - \beta_{\text{ppm}}\, r\hat{v}_\theta(r,\theta)\frac{\partial c^\alpha}{\partial \theta} + \frac{1}{Pe}\left[r^2\frac{\partial^2 c^\alpha}{\partial r^2} + r\frac{\partial c^\alpha}{\partial r} + \frac{\partial^2 c^\alpha}{\partial \theta^2}\right], \alpha = U, D. \tag{A3}$$

Substituting the representation 20 into equation, one obtains for the matrix representation $\mathbf{C}^\alpha(z) = (c^\alpha_{m,n}(z))^{N_{\text{F}}}_{m,n=0}, \alpha = U, D$ of the Fourier coefficients the linear system of equations

$$\mathbf{B}\frac{d\mathbf{C}^\alpha}{dz} = \beta_{\text{ppm}}\left(\mathbf{A}^{(1)} + \mathbf{A}^{(2)}\right)\mathbf{C}^\alpha - \frac{1}{\text{Pe}}\left(\mathbf{D}^{(1)} + \mathbf{D}^{(2)} + \mathbf{D}^{(3)}\right)\mathbf{C}^\alpha \alpha = U, D. \tag{A4}$$

If we set $c^r_m(r) = \cos(m\pi r)$, $s^r_m(r) = \sin(m\pi r)$, $c^\theta_n(\theta) = \cos(n\theta)$, $\sin^\theta_n(\theta) = \sin(n\theta)$, the matrices $\mathbf{B} = (B_{(m,n)(h,k)})^N_{m,h,n,k=0}$, and similarly for the others ($\mathbf{A}^{(1)}, \mathbf{A}^{(2)}, \mathbf{D}^{(1)}, \mathbf{D}^{(2)}, \mathbf{D}^{(3)}$), entering Eq. A4 are given by

$$B_{(m,n)(h,k)} = \int_0^1 dr \int_0^\pi r^2 w(r,\theta) c^r_m(r) c^r_h(r) c^\theta_n(\theta) c^\theta_k(\theta) d\theta,$$

$$A^{(1)}_{(m,n)(h,k)} = h\pi \int_0^1 dr \int_0^\pi r^2 \hat{v}_r(r,\theta) c^r_m(r) s^r_h(r) c^\theta_n(\theta) c^\theta_k(\theta) d\theta,$$

$$A^{(2)}_{(m,n)(h,k)} = k \int_0^1 dr \int_0^\pi r\hat{v}_\theta(r,\theta) c^r_m(r) c^r_h(r) c^\theta_n(\theta) s^\theta_k(\theta) d\theta,$$

$$D^{(1)}_{(m,n)(h,k)} = h^2\pi^2 \int_0^1 r^2 dr \int_0^\pi c^r_m(r) c^r_h(r) c^\theta_n(\theta) c^\theta_k(\theta) d\theta,$$

$$D^{(2)}_{(m,n)(h,k)} = h\pi \int_0^1 r dr \int_0^\pi c^r_m(r) s^r_h(r) c^\theta_n(\theta) c^\theta_k(\theta) d\theta,$$

$$D^{(3)}_{(m,n)(h,k)} = k^2 \int_0^1 r dr \int_0^\pi c^r_m(r) c^r_h(r) c^\theta_n(\theta) c^\theta_k(\theta) d\theta.$$

The matrices $\mathbf{B}, \mathbf{A}^{(k)}, k = 1, 2$ have been calculated in closed form by quadrature representing the velocity field on a very refined mesh, and using within each mesh element a bilinear interpolation for the velocity components. The matrices $\mathbf{D}^{(k)}$, $k = 1, 2, 3$ can be calculated in closed form.

As the second half modulus of the PPM basic unit is just a rotation of the first modulus by an angle $\pi/2$, instead of rewriting the advection–diffusion equations, it is more convenient to enforce this symmetry, and rotate the coordinate system by an angle $\pi/2$. Let $c^\alpha, \alpha = R, L$ be the representation of the concentration field in the second half unit (see Figure A1). The fields $c^L(r,\theta,z)$ and $c^R(r,\theta,z)$ can be expressed in Fourier series 20, and satisfy the balance Eq. A4. These two field at the inlet section of the second half unit $c^L(r,\theta,0)$ and $c^R(r,\theta,0)$ are related to the fields $c^U(r,\theta,1)$ and $c^D(r,\theta,1)$ of the first half unit by the equations

$$c^L(r,\theta,0) = \begin{cases} c^U(r,\theta+\pi/2,1) & \theta \in (0,\pi/2) \\ c^D(r,\theta+\pi/2,1) & \theta \in (\pi/2,\pi) \end{cases} \tag{A5}$$

$$c^R(r,\theta,0) = \begin{cases} c^U(r,\theta+\pi/2,1) & \theta \in (3\pi/2,2\pi) \\ c^D(r,\theta+\pi/2,1) & \theta \in (\pi,3\pi/2) \end{cases} \tag{A6}$$

By substituting the Fourier expansions 20 for the fields c^U, c^D, c^L, c^R into Eqs. A5–A6 a matrix equations for the Fourier coefficients can be obtained

$$\begin{pmatrix} \mathbf{C}^L(0) \\ \mathbf{C}^R(0) \end{pmatrix} = \begin{pmatrix} \mathbf{H}^{LU} & \mathbf{H}^{LD} \\ \mathbf{H}^{RU} & \mathbf{H}^{RD} \end{pmatrix} \begin{pmatrix} \mathbf{C}^U(1) \\ \mathbf{C}^D(1) \end{pmatrix}. \tag{A7}$$

The block matrix $\mathbf{H}$, the blocks of which are $\mathbf{H}^{LU}$, $\mathbf{H}^{LD}, \mathbf{H}^{RU}, \mathbf{H}^{RD}$ simply expresses the rotation of $\pi/2$ in the Fourier representation of the scalar field inside PPM at the cross-section separating the two half units.

Finally, to restore the initial orientational configuration at the exit cross section of the second half unit, a rotation of $-\pi/2$ should be performed in the Fourier representation. Let $\mathbf{K}$ be the block matrix representing this operation in the Fourier representation of the scalar field,

$$\mathbf{K} = \begin{pmatrix} \mathbf{K}^{UL} & \mathbf{K}^{UR} \\ \mathbf{K}^{DL} & \mathbf{K}^{DR} \end{pmatrix}. \tag{A8}$$

The matrix $\mathbf{K}$ is the inverse of the matrix $\mathbf{H}$. Let $\boldsymbol{\Gamma}$ be the matrix

$$\boldsymbol{\Gamma} = \mathbf{B}^{-1}\left[\beta_{\text{ppm}}\left(\mathbf{A}^{(1)} + \mathbf{A}^{(2)}\right) - \frac{1}{\text{Pe}}\left(\mathbf{D}^{(1)} + \mathbf{D}^{(2)} + \mathbf{D}^{(3)}\right)\right].$$

Gathering together these expressions, the matrix representation of the evolution operator $\mathbf{M}_G$, mapping the concentration field from the inlet to the outlet cross sections of a PPM unit is given by

$$\mathbf{M}_G = \begin{pmatrix} \mathbf{K}^{UL} & \mathbf{K}^{UR} \\ \mathbf{K}^{DL} & \mathbf{K}^{DR} \end{pmatrix} \begin{pmatrix} e^{\boldsymbol{\Gamma}} & 0 \\ 0 & e^{\boldsymbol{\Gamma}} \end{pmatrix} \begin{pmatrix} \mathbf{H}^{LU} & \mathbf{H}^{LD} \\ \mathbf{H}^{RU} & \mathbf{H}^{RD} \end{pmatrix} \begin{pmatrix} e^{\boldsymbol{\Gamma}} & 0 \\ 0 & e^{\boldsymbol{\Gamma}} \end{pmatrix}. \tag{A9}$$

Manuscript received Oct. 5, 2012, revision received Mar. 6, 2013, and final revision received Nov. 5, 2013.